Revision 4

Magma oxygen fugacity and volatile components control the Miocene high-Sr/Y granitoids forming either Cu or W mineralization in the Gangdese metallogenic region, Xizang, China

LI-QIANG WANG[1, 2*], TENG GAO[3], BAO-LIANG LI[1], YONG WANG[2]

[1] MNR Key Laboratory of Metallogeny and Mineral Assessment, Institute of Mineral Resources, Chinese Academy of Geological Sciences, Beijing 100037, China

[2] Chengdu University of Technology, Chengdu Sichuan 610059, China

[3] Zhaojin Mining Industry Company Limited, Zhaoyuan Shandong 265400, China

ABSTRACT: Porphyry copper deposits are usually associated with high-Sr/Y granitoids. The Miocene Gangdese porphyry copper belt in southern Tibet is also associated with high-Sr/Y granitoids, which also formed wolframite mineralizations. Why some coeval high-Sr/Y granitoids formed Cu deposits (Cu granitoids) whereas others formed W mineralizations (W granites) remains unclear. We attempt to address this issue by studying the magma sources and properties, analyzing magmatic zircons, biotites and apatites in theses granites, and combing this information with previously published bulk-rock and zircon isotopic data. In-situ chemical analyses of magmatic zircon, biotite and

* Corresponding author: Liqiang Wang (wlq060301@163.com)

apatite suggest that the properties of the magmas that produced the Cu granitoids and W granites were significantly different. Zircon ΔFMQ values of the W granites are much lower than those of the Cu granitoids, suggesting a more reduced magma for W mineralizations. Water content of the W granites (7-9 wt.%) seems to be lower than that of the Cu granitoids (10-12 wt.%). This is suggested by the low zircon Ce/Nd and (Ce/Nd)/Y ratios and high Dy/Yb ratios in the W granites. Biotite and apatite from the W granites generally have lower Cl contents than those from most Cu granitoids. Moreover, SO_3 content in apatite from the W granites is also lower than that from the Cu granitoids. These data agree with the genetic environment suggested by previously published isotopic data. Bulk-rock Sr-Nd and zircon Hf isotopes indicate that the Cu granitoids were mainly sourced from juvenile lower crust. In contrast, the source of W granites was contaminated with the old Lhasa terrane basement. Our results highlight the role of magma oxygen fugacity and volatile components in controlling metal variations in high-Sr/Y granitoids. Combinations of magmatic zircon ΔFMQ and Ce/Nd, (Ce/Nd)/Y and Dy/Yb ratios, and apatite and biotite SO_3 and Cl contents, can be used to discriminate W granites from Cu granitoids in the Gangdese metallogenic region, and hence granitoids potentially hosting W versus Cu ore deposits.

Keywords: High-Sr/Y granitoids, Porphyry copper deposit, W-related granites, Magma oxygen fugacity, Volatile components, Gangdese metallogenic region

INTRODUCTION

Porphyry copper deposits (PCDs) are generally associated with hydrous and oxidized magmas (Richards 2003), which can be generated in both magmatic arcs (Richards 2003; Sillitoe 2010) and collisional orogenic belts (Hou et al. 2015). Studies on PCDs, including cases in magmatic arcs and collisional zones worldwide, have proposed that the magmatic suites associated with PCDs usually have high-Sr/Y ratios (Richards and Kerrich 2007; Chiaradia et al. 2012; Richards et al. 2012; Loucks 2014). High-Sr/Y ratios may reflect residues of garnet and/or hornblende in the magma source region during partial melting or fractional crystallization of garnet and/or hornblende at high pressures above ~10 kbar (Loucks 2021). In addition, high-Sr/Y ratios can be generated in asthenosphere-derived arc magmas by upper plate crustal interaction and crystal fractionation (Richards and Kerrich 2007). The Gangdese porphyry copper belt (GPCB) in the southern Lhasa terrane (Fig. 1) is a typical collisional metallogenic belt and the PCDs in the GPCB are also associated with high-Sr/Y (> 20) and usually high-La/Yb (> 20) granitoids (Fig. 2) emplaced during the Miocene (22-12 Ma; Hou et al. 2015; Yang et al. 2016; Wang R. et al. 2018). Recently, several quartz vein- and greisen-type wolframite deposit and mineralization occurrences have been discovered in the northwestern GPCB; these deposits are genetically related to Miocene (14-11 Ma) high-Sr/Y and high-La/Yb biotite monzogranite and two-mica granite (Wang L.Q. et al. 2018, 2022; Wang Y. et al. 2020). They typically include the Jiaoxi deposit and the Jiaodong and Anglonggangri mineralization occurrences (Fig. 1b). These discoveries indicate that the Miocene

high-Sr/Y granitoids in the Gangdese metallogenic region formed not only Cu but also W deposits. The geological factors controlling the formation of distinct metal deposits by nearly coeval high-Sr/Y granitoids remain unclear. This is an important question that needs to be addressed because of its relationship with regional mineral resource prospecting and exploration.

The magma source and properties of granitoids (e.g., temperature, oxygen fugacity, sulfur fugacity, water content and halogen concentration) play key roles in controlling metal associations in magmatic-hydrothermal mineralization systems. Based on the oxygen fugacity (fO_2) estimated by bulk-rock chemical ratios (e.g., Fe^{3+}/Fe^{2+}, V/Cr and Eu^{3+}/Eu^{2+}) and amphibole oxybarometer, and the volatile component analysis of melt inclusions from magmatic rocks, the fertile magmas that form PCDs are considered hydrous, oxidized, and enriched in volatiles such as S and Cl (Sillitoe 2010; Richards 2015). A high magma water (H_2O) content is crucial for the generation of large volumes of ore-forming fluids in porphyries (Richards 2012; Loucks 2014). The high oxidation state of a porphyry keeps sulfur mainly in the form of SO_4^{2-} or SO_2 rather than S^{2-} in magmas. This facilitates the transport of Cu and prevents the early formation and precipitation of sulfides in magmatic-hydrothermal systems (Jugo 2009; Richards 2015). The importance of high magmatic S and Cl concentrations for PCDs lies in their capacity to make metals form complexing ligands, thereby efficiently promoting metal transport during magmatic-hydrothermal evolution (Chambefort et al. 2008; Chelle-Michou and Chiaradia 2017). Tungsten mineralizations, however, are usually associated with reduced

and F-rich granitic magmas, according to the low bulk-rock Fe_2O_3/FeO ratios and high F contents measured in ore-forming granites (Ishihara 1981, 2015; Harlaux et al. 2018; Azadbakht et al. 2020). Experimental studies have shown that W is dominantly present as W^{6+} in silicic magma (O'Neill et al. 2008). Although the fO_2 has little influence on the W^{6+} ion valence (Che et al. 2013), W is more prone to enter the magmatic-hydrothermal fluids and becoming enriched under low fO_2 conditions (Candela and Bouton 1990). Hence, W mineralization tends to be associated with reduced granites (Hart et al. 2004). Unlike Cu deposits commonly linked with Cl-rich magma and fluid, W mineralization preferentially occurs in F-rich magmatic-hydrothermal system (Vigneresse 2009; Ishihara 2015). High F contents may increase the abundance of nonbridging O atoms in melts (Keppler 1993), increasing the proportion of WO_4^{2-} in the melts (Che et al. 2013). Therefore, high F contents are important for promoting the enrichment of W in residual magmas (Che et al. 2013). Moreover, F can extend the magmatic evolution process and facilitate the migration of W in magmatic-hydrothermal systems (Vigneresse et al. 2011).

Biotite, apatite and zircon are modally abundant or frequent in felsic intrusions, and many studies have confirmed that the compositions of these minerals can be used to identify the physicochemical properties of their parent magma (Gardiner et al. 2017; Azadbakht et al. 2020). For instance, Ti-in-zircon thermometry has been widely used to calculate magma temperature (Ferry and Watson 2007). In addition, the Ti-Ce-U contents of zircon are useful indicators of the fO_2 of their host magmas (Loucks et al. 2020), and (Ce/Nd)/Y and Dy/Yb in zircon can provide H_2O content information about the magma

(Lu et al. 2016; Lee et al. 2021). Moreover, both biotite and apatite incorporate volatile components, such as H_2O, F, Cl and S (Boomeri et al. 2006; Webster and Piccoli 2015). Accordingly, they are useful for tracking the halogen concentrations and sulfur fugacity of magma (Mercer and Reed 2013; Bouzari et al. 2016; Li and Hermann 2017; Moshefi et al. 2018).

In this paper, we present in-situ major element analyses of biotite and apatite and trace element analyses of zircon from the W granites in the Jiaoxi, Jiaodong and Anglonggangri areas, to infer the properties of their associated magmas. These data, together with the published compositions of biotite, apatite and zircon from the Cu granitoids, and published bulk-rock Sr-Nd and zircon Hf isotopic analyses, provide insights into key factors controlling the formation of either Cu or W mineralization in Miocene high-Sr/Y granitoids in the Gangdese metallogenic region.

GEOLOGICAL SETTING

The Lhasa terrane (i.e. the Gangdese metallogenic region) is located in the southern Tibetan Plateau, south of and separated from the Qiangtang terrane by the Bangong-Nujiang suture zone. The Indus-Yarlung Zangbo suture zone to the south separates the Lhasa terrane from the Himalayan orogeny (Fig. 1). The Lhasa terrane can be subdivided into southern, central, and northern subterranes based on the different basement and sedimentary cover rocks (Zhu et al. 2013). The GPCB is located in the eastern part of the southern Lhasa subterrane, whereas the Jiaoxi, Jiaodong and Anglonggangri wolframite mineralization areas are situated in the western portion of the

125 northern Lhasa subterrane (Fig. 1b).

126 The southern Lhasa subterrane is bounded by the Indus-Yarlung Zangbo suture zone
127 to the south and by the Luobadui-Milashan fault to the north (Fig. 1). Precambrian
128 crystalline basement may be locally present east of this subterrane (Zhu et al. 2013). The
129 sedimentary cover is mainly composed of early Jurassic to Cretaceous volcano-sedimentary
130 strata with the local late Cambrian Nyningchi Group (Zhu et al. 2013). Magmatism in the
131 southern Lhasa subterrane is dominated by Late Triassic-Cretaceous Gangdese batholiths
132 and the Paleocene-Eocene Linzizong volcanic rocks (Mo et al. 2008; Ji et al. 2009). In
133 addition, post-collisional magmatic rocks (< 38 Ma) are widespread. They mainly consist
134 of small-volume Oligocene-Miocene (33-12 Ma) high-Sr/Y intrusions and Miocene (25-8
135 Ma) potassic-ultrapotassic volcanic rocks (Fig. 1b; Chung et al. 2003; Guo et al. 2007;
136 Liu D. et al. 2014). Among these post-collisional intrusions, the Miocene (22-12 Ma)
137 high-Sr/Y granodiorite and monzogranite porphyries are the ore-forming intrusions of
138 PCDs (Hou et al. 2015; Yang et al. 2016; Wang R. et al. 2018). The granodiorite porphyry
139 consists of plagioclase, K-feldspar, hornblende and quartz phenocrysts in a matrix of
140 quartz, plagioclase and biotite. Accessory minerals include apatite, zircon, titanite and
141 magnetite (Wang R. et al. 2015; Yang et al. 2016; Tang et al. 2021). The phenocrysts in
142 the monzogranite porphyry are quartz, plagioclase, K-feldspar and biotite with accessory
143 apatite, zircon, ilmenite and magnetite (Wu et al. 2016; Yang et al. 2016; Sun et al. 2018).

144 The northern Lhasa subterrane is located between the Bangong-Nujiang suture zone
145 and the Shiquanhe-Nam Tso mélange zone (Fig. 1). The oldest sequences in this

146 subterrane are found in the eastern part and contain middle to late Triassic sedimentary
147 strata interbedded with volcanic rocks (Zhu et al. 2013). These sequences are
148 unconformably overlain by middle to late Jurassic clastic rocks. Cretaceous strata
149 comprising sedimentary and volcanic rocks occur along the strike of this subterrane (Zhu
150 et al. 2013). The northern Lhasa subterrane is characterized by the presence of
151 widespread early Cretaceous granitoids, which are represented by the Anglonggangri,
152 AlongTso, Yanhu and Baingoin batholiths (Zhu et al. 2016). Furthermore, several late
153 Cretaceous and Paleocene-Eocene granites, as intrusions in the Anglonggangri batholith,
154 have been identified (Zhu et al. 2016). A previous study reported early Miocene (23 Ma)
155 high-Sr/Y trachytes to the west of the northern Lhasa subterrane (Guo et al. 2007). In
156 addition to trachytes, studies in the Jiaoxi, Jiaodong and Anglonggangri areas have shown
157 that Miocene high-Sr/Y granites do exist to the west of this subterrane (Wang L.Q. et al.
158 2022; Wang Y. et al. 2020).

159 The Jiaoxi deposit is composed of quartz vein- and greisen-type wolframite ores
160 (Wang L.Q. et al. 2018; Wang Y. et al. 2020). The Early Cretaceous Shiquanhe ophiolite
161 mélange, which contains sandstone, shale and sheets of ophiolitic rocks, is the main
162 geological body hosting the quartz vein-type wolframite ores (Fig. S1). Several Miocene
163 intrusions, including the high-Sr/Y porphyritic biotite monzogranite (14.1 Ma) and the
164 more evolved granite porphyry (13.8 Ma) and muscovite granite (13.7 Ma), have been
165 recognized (Wang L.Q. et al. 2018; Wang Y. et al. 2020). The greisen-type wolframite
166 ores are widely developed in the muscovite granite, with minor occurrences in the altered

167 porphyritic biotite monzogranite.

168 The Jiaodong wolframite mineralization is near the Jiaoxi deposit and shows similar
169 associated geological units (Fig. S2). The Early Cretaceous Shiquanhe ophiolite mélange
170 was intruded by the high-Sr/Y (porphyritic) biotite monzogranite pluton (14.2 Ma), with
171 numerous pegmatite veins and local two-mica granite and muscovite granite dikes (Wang
172 L.Q. et al. 2018). The pegmatite veins cutting through the biotite monzogranite have
173 muscovite ^{40}Ar-^{39}Ar plateau ages of 10.2 Ma (Wang L.Q. et al. 2022). The wolframite
174 mineralization exists as veinlets or disseminated styles in the pegmatite and muscovite
175 granite. Geochronology, bulk-rock geochemistry and Sr-Nd-Hf isotope studies suggest
176 that these intrusions in the Jiaoxi and Jiaodong areas are cogenetic and originated from
177 the same magma source (Wang Y. et al. 2020).

178 The Anglonggangri wolframite mineralization area is located northeast of the Jiaoxi
179 deposit (Fig. 1). The strata in this area are the middle-late Jurassic Lagongtang Formation
180 and the early Cretaceous Duoni Formation (Fig. S3). The Lagongtang Formation consists
181 of sandstones, siltstones and slates and is unconformably overlain by slates of the Duoni
182 Formation. Intrusions in the area are divided into two episodes, i.e., the late Cretaceous
183 syenogranite and granodiorite and the Miocene high-Sr/Y two-mica granite (11.1-10.7
184 Ma), garnet-muscovite granite (10.2 Ma) and pegmatite (Wang L.Q. et al. 2022). The W
185 mineralization is developed in a vein-like style in the two-mica granite. Geochronology,
186 bulk-rock geochemistry, and Sr-Nd-Pb-Hf isotope results of the intrusions indicate that
187 they are cogenetic and that the two-mica granite represents the parent magma of the

188 highly evolved garnet-muscovite granite and pegmatite (Wang L.Q. et al. 2022).

189 **SAMPLING AND ANALYTICAL METHODS**

190 **Sample description**

191 The biotite monzogranite and two-mica granite, which represent the less evolved
192 endmembers and parent magmas in their mineralized areas, are the focus of this study.
193 The biotite monzogranite samples were collected from outcrops in the Jiaoxi and
194 Jiaodong areas and from a drill core in the Jiaoxi deposit. The two-mica granite samples
195 were collected from outcrops in the Jiaodong and Anglonggangri areas. The detailed
196 petrographic features of these rocks and the characteristics of the minerals studied here
197 are provided below and in Wang L.Q. et al. (2018, 2022) and Wang Y. et al. (2021).

198 **Biotite monzogranite**

199 The biotite monzogranite is porphyritic and consists predominantly of quartz (~25%),
200 K-feldspar (~35%), plagioclase (~30%) and biotite (~10%), with accessory zircon, apatite,
201 monazite and ilmenite (Fig. S4a-b). The biotite crystals (0.3-1.0 mm) exhibit a green
202 color (replaced by chlorite due to alteration; Fig. 3a) and contain abundant inclusions of
203 apatite, ilmenite and monazite (Fig. 3b). Hydrothermal alteration in the biotite
204 monzogranite is extensive and strong. The K-feldspar and plagioclase crystals are
205 commonly altered to sericite, and the biotite crystals are almost completely replaced by
206 chlorite and muscovite (Fig. 3a). Apatite crystals are mainly present as inclusions in
207 biotite; they are subhedral and have sizes of 20-50 μm (Fig. 3c-d). Although under the
208 optical microscope, apatites appear to develop corrosion edges, high-magnification

backscattered electron (BSE) images show that they are mostly homogeneous and have very few mineral and fluid inclusions (Fig. 3c-d). These characteristics suggest that these apatites are likely of magmatic origin and crystallized before fluid exsolution.

Two-mica granite

The two-mica granite is medium- to coarse-grained and comprises mainly quartz (~30%), plagioclase (~40%) and K-feldspar (~20%), with minor biotite (~5%) and muscovite (~5%) (Fig. S4c-d). The accessory mineral assemblage is similar to that of the biotite monzogranite and includes zircon, monazite, apatite and ilmenite. Minerals in most of the granite have not undergone hydrothermal alteration. The euhedral to subhedral biotite crystals are commonly ~0.5 × 2.0 mm in size and show clear differences from the fine-grained scaly biotite aggregates that re-equilibrate with exsolved fluids. A reddish-brown color (Fig. 3f, k) may indicate moderately oxidized to reduced conditions during growth (Lalonde and Bernard 1993). The biotite crystals often contain zircon, apatite and ilmenite inclusions (Fig. 3g, l), suggesting early crystallization. The zircon crystals included in apatite suggest that zircon crystallized earlier than apatite (Fig. 3f-g). Apatites appear mainly as individual crystals in the matrix (Fig. 3g) or are hosted in biotite (Fig. 3l). They are generally larger and more euhedral compared to those in the biotite monzogranite and typically show magmatic microstructures such as homogeneous euhedral crystals without fluid inclusions or hydrothermal alteration (Fig. 3h-i, m-n).

Analytical methods

Petrographic studies of 15 biotite and 25 apatite crystals were carried out on 15

polished thin sections using polarization microscopy and BSE imaging. Electron microprobe analysis (EMPA) of major elements in biotite and apatite was carried out using a JEOL JXA-8230 electron microprobe at the Institute of Mineral Resources, Chinese Academy of Geological Sciences, Beijing. To overcome spectral interferences between F$K\alpha$ of the synthetic W-Si multi-layered pseudocrystals (LDE1) and Fe$K\alpha$ of Fe-bearing minerals, the method of Zhang et al (2016) was adopted to accurately measure F concentration in biotite. The operating conditions were as follows: 15 kV accelerating voltage, 20 nA beam current, and 5 μm beam spot; a ZAF correction procedure for data reduction was used. The following minerals and synthetic oxides were used for calibration: K-feldspar (K), jadeite (Na, Al, Si), apatite (Ca, P), hematite (Fe), pyrope garnet (Mg), $MnTiO_3$ (Mn), rutile (Ti), topaz (F), barite (S), and halite (Cl). The detection limits for Cl and SO_3 are 90 ppm and 200 ppm, respectively.

The zircon crystals analyzed for trace elements were collected from the Jiaoxi (Fig. 3e) and Jiaodong biotite monzogranites (Fig. 3j) and the Anglonggangri two-mica granite (Fig. 3o), with ages of 14-11 Ma. The trace elements of zircons were measured using a Thermo Fisher's X-Series II inductively coupled plasma-mass spectrometry (ICP-MS) instrument attached to a GeoLasPro-193 nm laser system at the State Key Laboratory of Geological Processes and Mineral Resources, China University of Geoscience, Beijing. Helium was used as the carrier gas and was mixed with argon prior to entering the ICP-MS torch. All the data were acquired in single post ablation mode at a spot size of 32 μm with a frequency of 6 Hz. The standard materials SRM610 glass and ^{29}Si were used

as the external and internal standards, respectively. Standard materials were analyzed once after every ten analyses on the studied sample. Each analysis included a background acquisition of 20 s (gas blank) followed by 50 s of data acquisition from the sample. Quantitative calibration for trace element analyses was performed by ICPMSDataCal.

Methods for magma temperature and fO_2 estimation

The magma temperatures were calculated using the Ti-in-zircon thermometer ($T_{Ti\text{-}Zr}$) of Ferry and Watson (2007), assuming that α_{SiO2} = 1.0 and α_{TiO2} = 0.7 based on the presence of quartz and ilmenite in the W granites. In addition to the mineral geothermometer, bulk-rock geochemistry of the granitoids was also used to constrain the magma temperature. The solubility of zircon in granitic melt is controlled by temperature and M [= (Na +K +2Ca)/(Al × Si)] (molar contents; Boehnke et al., 2013). When M is < 2.1, the bulk-rock zircon concentration can be used to estimate the magma temperature through the zircon saturation thermometry (T_{Zr}) of Watson and Harrison (1983). The oxidation states of the W granites were assessed using the bulk-rock ferric/ferrous ratios (Fe_2O_3/FeO) and zircon oxybarometer of Loucks et al. (2020).

RESULTS

Mineral compositions

Biotite composition

The major elements and halogen contents of the examined biotite crystals are presented in Table S1. Geochemical data were not obtained for biotite in the Jiaoxi and Jiaodong biotite monzogranites due to the extensive hydrothermal alteration of biotite to

chlorite. The chemical composition of biotite was calculated based on 22 atoms of oxygen per formula unit (Table S1).

Biotite from the Anglonggangri two-mica granite has relatively uniform SiO_2 (34-39 wt.%), Al_2O_3 (16.4-18.5 wt.%), FeO (21.1-22.9 wt.%) and MgO (5.1-6.5 wt.%) contents but large variations in TiO_2 (1.4-3.2 wt.%) and SO_3 (200-690 ppm) concentrations. Biotites have F concentrations of 4040-11430 ppm and Cl concentrations of 90-350 ppm. Compared to that from the Anglonggangri two-mica granite, the biotite from the Jiaodong two-mica granite has higher SiO_2 (39-41 wt.%) and Al_2O_3 (17.6-19.2 wt.%) contents but lower TiO_2 (1.1-1.8 wt.%), FeO (16.8-19.5 wt.%) and MgO (4.1-5.0 wt.%), with similar SO_3 concentrations (200-530 ppm; Fig. 4a). The F (9200-17140 ppm) and Cl (90-1930 ppm) concentrations are greater than those in the Anglonggangri two-mica granite (Fig. 4b-c). The higher SiO_2, Al_2O_3 and F contents and lower FeO and MgO contents of biotite from the Jiaodong two-mica granite suggest that this granite is more evolved than the Anglonggangri two-mica granite (Azadbakht et al. 2020). The Fe/(Fe+Mg) ratios and total aluminum content (ΣAl) of biotite increase from the Anglonggangri to Jiaodong two-mica granite (Fig. 4d), further reflecting an increasing degree of fractionation of their host magmas (Azadbakht et al. 2020). According to the classification diagram of the International Mineralogical Association (Rieder et al. 1998), the Jiaodong and Anglonggangri biotites are categorized as siderophyllite (Fig. 4d).

Apatite composition

Table S2 presents the geochemical compositions of the apatite crystals. To minimize

293 the F and Cl migration effect during EMPA (Goldoff et al. 2012; Stock et al. 2015), only
294 the data from apatite crystals with elongated hexagonal shapes, indicating that the
295 analytical plane was parallel or oblique to the c-axis of the apatite crystals, were studied.
296 The CaO and P_2O_5 of apatite in the biotite monzogranite account for 52-55 wt.% and
297 38-42 wt.%, respectively. The MnO concentration (80-7620 ppm) in apatite from the
298 biotite monzogranite show significant variations, whereas the F contents (24770-37460
299 ppm) are less variable (Fig. 5). Almost all the apatite crystals have Cl and SO_3
300 concentrations below the detection limits. The apatite in the two-mica granite has CaO
301 (53-56 wt.%) and P_2O_5 (39-44 wt.%) contents similar to those in the biotite monzogranite.
302 In contrast, the MnO (970-8700 ppm) concentrations increase from the biotite
303 monzogranite to the two-mica granite, whereas the F (14380-36490 ppm) concentrations
304 decrease (Fig. 5). Concentrations of SO_3 and Cl in most apatite crystals are below the
305 detection limits, with a few samples containing SO_3 and Cl concentrations of 200-3790
306 and 90-410 ppm, respectively.

307 **Zircon trace element composition**

308 Only the trace elements for zircons of Miocene U-Pb ages with concordance > 90%
309 were selected for this study. The trace element compositions of zircon crystals are provided
310 in Table S3. Zircon data with La > 0.1 ppm indicating LREE-rich mineral contamination
311 (Zou et al. 2019), and Ti > 50 ppm reflecting Ti oxide contamination (Lu et al. 2016),
312 were excluded. Zircons from the W granites are characterized by total rare earth element
313 (ΣREE) concentrations of 136-1725 ppm. They are enriched in HREE with positive Ce

314 anomalies (Fig. S5), which are typical features of magmatic zircons (Hoskin and
315 Schaltegger 2003). The Ti concentrations in zircons from the W granites range between 1
316 and 24 ppm. The crystallization temperatures calculated for zircons from the biotite
317 monzogranite (653-876°C, average = 777°C) and two-mica granite (721-840°C, average
318 = 777°C) are similar. Zircons from the W granites have moderate to low Eu/Eu^* (0.1-0.6,
319 mostly ≤ 0.4), Ce/Nd (0.9-11.5, mostly < 5) and Dy/Yb ratios (0.3-0.7, mostly > 0.4).

320 **Properties of W granites**

321 The magma properties and partial key parameters of the W granites are summarized
322 and presented in Table 1.

323 **Temperatures of magma**

324 The average crystallization temperature for zircons from the biotite monzogranite
325 and two-mica granite using the Ti-in-zircon thermometer is 777°C. Based on previously
326 published bulk-rock geochemistry data (Table S4; Wang Y. et al. 2020; Wang L.Q. et al.
327 2022), the T_{Zr} temperatures calculated for the biotite monzogranite (M = 1.0-1.4) and
328 two-mica granite (M = 1.3-1.4) are 751-829°C (average = 784°C) and 711-768°C
329 (average = 736°C), respectively. The average temperatures calculated for the W granites
330 by these two methods are consistent within error (± 50°C; Ferry and Watson 2007).

331 **Magma oxygen fugacity**

332 Due to the extensive and strong alteration of the Jiaoxi biotite monzogranites, fO_2
333 estimation using bulk-rock Fe_2O_3/FeO ratios was not carried out here. The Jiaodong
334 biotite monzogranite and Anglonggangri two-mica granite have relatively low Fe_2O_3/FeO

values. They plot below the nickel-nickel (NNO) buffer line in the Fe_2O_3/FeO vs. SiO_2 diagram (Fig. 6a), with most data points in the range of Sn-W deposits (Hart et al. 2004). Based on the zircon oxybarometer, $\log fO_2$ values calculated for the Jiaoxi and Jiaodong biotite monzogranites range from -19.6 to -13.8 (average = -15.5). The Anglonggangri two-mica granite shows slightly lower $\log fO_2$ values from -21.4 to -14.1 (average = -16.3). In the zircon $T_{Ti\text{-}Zr}$ vs. $\log fO_2$ diagram (Fig. 6b), the majority of the W granites data points plot below the NNO line, indicating that they formed under relatively reducing condition. Extremely low ΔFMQ values for five zircons from the W granites (-4.8~-2.9), associated with high U concentrations, are not included in the following discussion. The calculated zircon ΔFMQ values for the biotite monzogranite and two-mica granite vary from -2.1 to 2.4 (average = 0.2) and from -2.2 to 0.6 (average = -0.8), respectively. The low zircon ΔFMQ values also suggest that the W granites formed under reducing condition (Fig. 6c).

Magma water content

Zircons with (Ce/Nd)/Y > 0.01 and Dy/Yb < 0.3 have been proposed to indicate high water contents (up to 12 wt.%) in the magma (Lu et al. 2015, 2016). Although nearly half of the zircon (Ce/Nd)/Y ratios from the biotite monzogranite are greater than 0.01 (Fig. 7a), almost all the Dy/Yb ratios of zircons from the W granites are higher than 0.3 (Fig. 7b-c). These trace element compositions of zircon may suggest that the magmas from which the zircon crystallized were relatively low in H_2O. The discussion of the magma source below, together with a previous study by Wang L.Q. et al (2022), shows that the W granites were likely generated by dehydration melting of garnet amphibolite in

the lower crust at high pressure (maybe > 12 kbar). Accordingly, a garnet amphibolite sample from the eastern Himalayan syntaxis (LZ06-20-4; Kang et al. 2020) was selected for phase equilibrium modeling to estimate the magma H_2O content by using the software GeoPS of Xiang and Connolly (2022). To obtain more complete information on the magma H_2O content, a relatively large range of pressure (8.2-16.6 kbar) and temperature conditions (720-900 °C) similar to those of the W granites, were investigated during phase equilibrium modeling. The magma H_2O content results vary from 8.6 wt.% at 720°C and 8.2 kbar to 6.9 wt.% at 900°C and 16.6 kbar (Fig. 7d), with an average value of 7.7 wt.%. The average magma H_2O content estimated here is consistent with that from previous experimental studies (6.7 ± 1.4 wt.%; Sen and Dunn 1994; Rapp and Watson 1995; Sisson et al. 2005). Hence, we infer that the H_2O contents in the W granites magmas at or close to the source region were approximately between 7 and 9 wt.%.

Magma halogen fugacity

The average F contents of biotite from the Anglonggangri and Jiaodong two-mica granites are 0.35 atoms per formula unit (apfu) and 0.69 apfu, respectively. The average Cl contents are 0.007 and 0.004 apfu for biotite from the Jiaodong and Anglonggangri two-mica granites, respectively. The Mg/Fe ratio of the octahedral site is an important factor affecting F and Cl contents in magmatic biotite (Azadbakht et al. 2020). To normalize this influence, the intercept values IV(F), IV(Cl) and IV(F/Cl) of biotite defined by Munoz (1984) were used to reveal the degree of halogen enrichment in magmas. The Anglonggangri biotite has IV(F) values of 1.49-1.90 with an average of

1.67, whereas the Jiaodong biotite has an average IV(F) value of 1.37. In addition, the Anglonggangri biotite has a slightly higher average IV(Cl) value (-2.55) than the Jiaodong biotite (-2.58). Moreover, the IV(F) and IV(F/Cl) values roughly correlate positively, and most data plot in or close to the Sn-W-Be deposit field in the biotite IV(F/Cl) vs. IV(F) diagram (Fig. 8).

A thermodynamic equation was used to estimate the Cl content of melt in equilibrium with apatite (Li and Hermann 2017). The equation is Cl_{melt} (wt.%) = $X_{Cl}^{Ap}/X_{OH}^{Ap}\times(1/Kd_{Cl\text{-}OH}^{Ap\text{-}melt}) \times 10.79$ and $Kd_{Cl\text{-}OH}^{Apatite\text{-}melt} = e^{(25.81 + (XClAp\text{-}XOHAp) \times 17.33) \times (1000/8.314/T)}$, with the temperature (T) in K. According to this equation, the average Cl contents calculated for the magmas of the biotite monzogranite and two-mica granite are 0.01% and 0.03%, respectively. The results suggest that the W granites are low in Cl. This is in agreement with the low Cl contents measured in apatite (Fig. 5).

DISCUSSION

The composition of magmatic biotite, apatite and zircon have been used to investigate physicochemical information on their associated ore-forming granitoids for PCDs, whereas their application to the W ore-forming granites is relatively rare. The compositions of biotite (Fe^{3+}-Fe^{2+}-Mg^{2+}), apatite (Mn) and zircon (Eu and Ce anomalies and Ce^{4+}/Ce^{3+}) have been widely analyzed to indicate the high fO_2 conditions or H_2O contents of granitoids for PCDs (e.g., Ballard et al., 2002; Wang et al., 2014; Gardiner et al., 2017; Azadbakht et al., 2020; Yu et al., 2022). However, recent studies have argued that these mineral indicators are not robust enough to reflect the fO_2 of ore-forming

398 granitoids (Marks et al., 2016; Loucks et al., 2020; Loader et al., 2022); therefore, the
399 zircon oxybarometer of Loucks et al. (2020) is used here. In contrast, it is generally
400 accepted that the high halogen and SO_3 contents of biotite and apatite can reflect the high
401 Cl and S fugacity of fertile granitoids for PCDs (e.g., Chelle-Michou and Chiaradia, 2017;
402 Moshefi et al., 2018; Zhu et al., 2018).

403 **Different properties between W and Cu granitoids**

404 Based on the Ti-in-zircon thermometer (Ferry and Watson 2007), the crystallization
405 temperatures calculated for zircons from the Cu granitoids range from 651°C to 783°C
406 (average = 686°C; Table S7). These calculations show that most of the Cu granitoids have
407 lower temperatures than the W granites (Fig. 6b). This is compatible with the interpretation
408 that the Gangdese Cu granitoids are higher in H_2O with respect to the W granites.

409 The available bulk-rock Fe_2O_3/FeO ratios (Zheng et al. 2020 and references therein)
410 show that almost all the Cu granitoids plot above the NNO line (Fig. 6a), indicating their
411 formation under moderate to strong oxidizing conditions. In contrast, all the W granites
412 are located below the NNO line, showing more reduced conditions (Fig. 6a). Higher fO_2
413 values in the Cu granitoids compared to the W granites is further supported by the zircon
414 oxybarometer of Loucks et al. (2020). The logfO_2 values calculated for zircons from the
415 Cu granitoids range from -18.6 to -12.2 (Table S7). As shown in the zircon logfO_2 vs.
416 $T_{Ti\text{-}Zr}$ diagram (Fig. 6b), most Cu granitoids plot above the NNO buffer line. However, the
417 majority of the W granites data points plot below the NNO line (Fig. 6b). These
418 differences indicate that the magmas from which the PCDs formed were more oxidized

than magmas that formed the W granites. Moreover, the Cu granitoids have zircon ΔFMQ values of -0.8 to 4.1, which are clearly higher than those of the W granites (Fig. 6c). Based on all the above results, it is proposed that the Cu granitoid magmas were characterized by higher fO_2 than the W granite magmas.

The H_2O content in the source area of the W granite magmas is estimated to be 7-9 wt.% (Fig. 7d). Zircons from both the Cu and W granitoids have similar Eu/Eu^* ratios, but their Ce/Nd, (Ce/Nd)/Y and Dy/Yb ratios are significantly different (Fig. 7a-c). The higher zircon (Ce/Nd)/Y (> 0.01) and Ce/Nd (> 10) ratios and lower Dy/Yb (< 0.3) ratios of the Cu granitoids suggest higher H_2O contents in the Cu granitoid magmas than in the W granite magmas (Fig. 7a-c). This is supported by the wt% H_2O estimates of the Cu granitoids from Lu et al. (2015). Based on zircon saturation thermometry combined with phase equilibria (Clemens et al. 1986), the minimum magma H_2O content in the Cu granitoid magmas is estimated to be 10-12 wt.% (Lu et al. 2015). This high H_2O content has been attributed to the addition of H_2O from mantle-derived ultrapotassic melts (Yang et al. 2015, 2016).

The F and Cl concentrations of magmatic biotite and apatite crystals were used to compare the magma halogen fugacity of the Cu and W granitoid magmas. The biotite from the Cu granitoids has lower F contents but higher Cl contents (> 0.03 wt.%) than that from the W granites (Fig. 4b-c). The apatite crystals from the Cu granitoids have F concentrations similar to those from the W granites (Fig. 5a-b). However, the Cu granitoids contain apatites with much higher Cl contents (> 0.05 wt.%) (Fig. 5a-b). The

440 halogen compositions show that the fertile magmas for the Gangdese PCDs are enriched
441 in Cl. Compared with the W granites, the Cu granitoids also exhibit greater sulfur
442 fugacity, as shown by their higher apatite SO_3 contents (> 0.04 wt.%; Fig. 5c-d).
443 Although SO_3 contents of some apatites from the W granites also exceed 0.04 wt.%, most
444 of them have lower SO_3 concentrations (< 0.02 wt. %) than those of the Cu granitoids.

445 **Magma oxygen fugacity and volatile components control the metal variations**

446 The properties of the source and magma generated are important factors in
447 controlling the metal associations in magmatic-hydrothermal mineralization systems
448 (Hart et al. 2004; Sillitoe 2010; Richards 2015). Constraints on the source regions and
449 magma properties associated with the Gangdese Cu and W granitoids can clarify the
450 critical factors controlling their different metal element associations.

451 Zircon Hf and bulk-rock Sr-Nd isotope data previously collected (Wang Y. et al.
452 2020; Wang L.Q. et al. 2022; Zheng et al. 2020 and references therein) are used to
453 compare the magma sources of the Cu and W granitoids. Both the Cu and W granitoids
454 display wide ranges of zircon $\varepsilon_{Hf}(t)$ values (Fig. 9a) and Hf isotope two-stage model ages
455 (T_{DM}^{C}; Fig. 9b), indicating mixed magma sources. The depleted zircon $\varepsilon_{Hf}(t)$ (> 5) and
456 young T_{DM}^{C} (< 600 Ma) of the Cu granitoids were generated from mantle-derived juvenile
457 lower crust (Chung et al. 2003; Hou et al. 2015). However, the non-radiogenic zircon
458 $\varepsilon_{Hf}(t)$ (< 0) and ancient T_{DM}^{C} values (> 1000 Ma) of the W granites suggest that their
459 source region was contaminated with the Lhasa terrane basement. The bulk-rock Sr-Nd
460 isotopes also support magma source mixing between a juvenile component and ancient

basement material. In the $(^{87}Sr/^{86}Sr)_i$ vs. SiO_2 diagram (Fig. 9c), a crustal assimilation (CA) process is suggested. To further clarify the contributions of the basement materials during magma formation, the Cretaceous gabbro in the southern Lhasa subterrane (09TB79; Ma et al. 2013) was assumed to represent the juvenile lower crust, and the Cambrian Amdo gneiss (G118A and G118D; Harris et al. 1988a, b) was selected as the basement material for binary mixing during partial melting. All the Cu and W granitoids plot along a binary mixing line (Fig. 9d). This diagram shows potentially much greater contributions (30-60%) of the Lhasa terrane basement materials to the W granites than to the Cu granitoids (mostly < 40%; Fig. 9d).

Figure 9 suggests that the combination of partial melting of juvenile lower crust and mixing (0-50%) with gneiss-derived crustal melts, formed the oxidized hydrous and S-enriched Cu granitoids in the Miocene Gangdese metallogenic region (Fig. 10; Hou et al. 2015; Yang et al. 2016). Compared to the Cu granitoids, the coeval W granites were more reduced and S and Cl poor, which is compatible with a higher degree of contamination (30-60%) from the Lhasa terrane basement in the magma source (Fig. 10). Although the W granites were likely hydrous, containing approximately 7-9 wt.% water, the H_2O contents of the W granites were likely lower than those of the Cu granitoids (Fig. 7a-c). The relatively reduced condition and lower H_2O, Cl and S contents of the W granites hindered the sufficient transport of metals to form PCDs. However, the more reduced magma favored the genesis of W mineralizations. In addition, (garnet) muscovite granite and pegmatite are developed in the W mineralized areas, and they are highly

evolved phases of the W granites. The high degrees of magma evolution also promoted W enrichment and mineralization in the late magma stages.

IMPLICATIONS FOR TUNGSTEN EXPLORATION

There are large volumes of Miocene high-Sr/Y granitoids in the Gangdese region, and they have formed both PCDs and quartz vein and greisen type wolframite deposits. It is very important to discriminate between granitic suites fertile for either Cu or W mineralization, both for prospecting and exploration directions in new areas, and to avoid economic losses potentially caused by incorrect exploration.

When comparing the Cu granitoids and W granites, the later are more reduced and less hydrous and have low magmatic sulfur and chlorine fugacity. Hence, when exploring for tungsten mineralization, this study suggests to determine the reduced character of the related granites by obtaining zircon ΔFMQ values (< 0) and bulk-rock Fe_2O_3/FeO ratios (< 0.3), and the less hydrous character of granites by measuring the zircon Ce/Nd/Y (< 0.01), Ce/Nd (< 10) and Dy/Yb (> 0.3) ratios. In addition, the low magmatic sulfur and chlorine features of granites should be determined by measuring SO_3 and Cl contents (< 0.04 wt.% and < 0.05 wt.%, respectively) in magmatic apatite and the Cl contents in magmatic biotite (Cl < 0.03 wt.%).

FUNDING

This research was financially supported by the National Key R&D Program of China (2021YFC2900100), the National Natural Science Foundation of China (41873046) and the China Geological Survey (DD20240078, DD20230360).

ACKNOWLEDGEMENTS

We thank the associate editors Antonio Acosta-Vigil and Allen Schaen and the editor Don R. Baker and Thomas Lamont and the anonymous reviewers for their thoughtful and constructive comments that improved this manuscript greatly.

REFERENCES CITED

Azadbakht, Z., Lentz, D.R, McFarlane, C.R.M., and Whalen, J.B. (2020) Using magmatic biotite chemistry to differentiate barren and mineralized Silurian-Devonian granitoids of New Brunswick, Canada. Contributions to Mineralogy and Petrology, 175, 69.

Ballard, J.R., Palin, M.J., and Campbell, I.H. (2002) Relative oxidation states of magma inferred from Ce(IV)/Ce(III) in zircon: Application to porphyry copper deposits of northern Chile. Contributions to Mineralogy and Petrology, 144, 347-364.

Boehnke, P., Watson, E.B., Trail, D., Harrison, T.M., and Schmitt A.K. (2013) Zircon saturation re-revisited. Chemical Geology, 351, 324-334.

Boomeri, M., Mizuta, T., Ishiyama, D., and Nakashima, K. (2006) Fluorine and chlorine in biotite from the Sarnwosar granitic rocks, Northeastern Iran. Iranian Journal of Science & Technology, 30, 111-125.

Bouzari, F., Hart, C.J.R., Bissig, T., and Barker, S. (2016). Hydrothermal alteration revealed by apatite luminescence and chemistry: A potential indicator mineral for exploring covered porphyry copper deposits. Economic Geology, 111, 1397-1410.

Candela, P.A., and Bouton, S.L. (1990) The influence of oxygen fugacity on tungsten and molybdenum portioning between silicate melts and ilmenite. Economic Geology, 85,

633-640.

Chambefort, I., Dilles, J.H., and Kent, A.J.R. (2008) Anhydrite-bearing andesite and dacite as a source for sulfur in magmatic-hydrothermal mineral deposit. Geology, 36, 719-722.

Che, X.D., Linnen, R.L., Wang, R.C., Aseri, A., and Thibault, Y. (2013) Tungsten solubility in evolved granitic melts: An evaluation of magmatic wolframite. Geochimica et Cosmochimica Acta, 106, 84-98.

Chelle-Michou, C., and Chiaradia, M. (2017) Amphibole and apatite insights into the evolution and mass balance of Cl and S in magmas associated with porphyry copper deposit. Contributions to Mineralogy and Petrology, 172, 1-26.

Zhang, C., Koepke, J., Wang, L.X., Wolff, P.E., Wilke, S., Stechern, A., Almeev, R., and Holtz, F. (2016) A practical method for accurate measurement of trace level fluorine in Mg- and Fe-bearing minerals and glasses using electron probe microanalysis. Geostandards and Geoanalytical Research, 40, 351-363.

Chiaradia, M., Ulianov, A., Kouzmanov, K., and Beate, B. (2012) Why large porphyry Cu deposits like high-Sr/Y magmas? Scientific Reports, 685, 1-7.

Chung, S.L., Liu, D., Ji, J., Chu, M.F., Lee, H.Y., Wen, D.J., Lo, C.H., Lee, T.Y., Qian, Q., and Zhang, Q. (2003) Adakites from continental collision zones: Melting of thickened lower crust beneath southern Tibet. Geology, 31, 1021-1024.

Ferry, M., and Watson, E.B. (2007) New thermodynamic models and revised calibrations for the Ti-in-zircon and Zr-in-rutile thermometers. Contributions to Mineralogy and

545 Petrology, 154, 429-437.

546 Gardiner, N.J., Hawkesworth, C.J., Robb, L.J., Whitehouse, M.J., Roberts, N.M.W.,
547 Kirkland, C.L., and Evans, N.J. (2017) Contrasting granite metallogeny through the
548 zircon record: A case study from Myanmar. Scientific Reports, 748, 1-9.

549 Goldoff B., Webster J.D., and Harlov, D.E. (2012) Characterization of fluor-chlorapatites
550 by electron probe microanalysis with a focus on time-dependent intensity variation
551 of halogens. American Mineralogist, 97, 1103-1115.

552 Guo, Z.F., Wilson, M., and Liu, J.Q. (2007) Post-collisional adakites in south Tibet:
553 Products of partial melting of subduction-modified lower crust. Lithos, 96, 205-224.

554 Harlaux, M., Romer, R.L., Mercadier, J., Morlot, C., Marignac, C., and Cuney, M. (2018)
555 40 Ma years of hydrothermal W mineralization during the Variscan orogenic
556 evolution of the French Massif Central revealed by U-Pb dating of wolframite.
557 Mineralium Deposita, 53, 21-51.

558 Harris, N.B.W., Xu, R.H., Lewis, C.L., Hawkesworth, C.J., and Zhang, Y.Q. (1998a)
559 Isotope geochemistry of the 1985 Tibet geotraverse, Lhasa to Golmud: Philosophical
560 Transactions of the Royal Society of London. Series A, Mathematical and Physical
561 Sciences, 327, 263-285.

562 Harris, N.B.W., Xu, R.H., Lewis, C.L., and Jin, C.W. (1988b) Plutonic rocks of the 1985
563 Tibet geotraverse, Lhasa to Golmud: Philosophical Transactions of the Royal
564 Society of London. Series A, Mathematical and Physical Sciences, 327, 145-168.

565 Hart, C.J.R., Mair, J.L., Goldfarb, R.J., and Groves, D.I. (2004) Source and redox

controls on metallogenic variations in intrusion-related ore systems, Tombstone-Tungsten Belt, Yukon Territory, Canada. Transactions of the Royal Society of Edinburgh: Earth Sciences, 95, 339-356.

Hoskin, P.W., and Schaltegger, U. (2003) The composition of zircon and igneous and metamorphic petrogenesis. Reviews in Mineralogy and Geochemistry, 53, 27-62.

Hou, Z.Q., Zheng, Y.C., Zeng, L.S., Gao, L.E., Huang, K.X., Li, W., Li, Q.Y., Fu, Q., Liang, W., and Sun, Q.Z. (2012) Eocene-Oligocene granitoids in southern Tibet: Constraints on crustal anatexis and tectonic evolution of the Himalayan orogen. Earth and Planetary Science Letters, 349-350, 38-52.

Hou, Z.Q., Yang, Z.M., Lu, Y.J., Kemp, A., Zheng, Y.C., Li, Q.Y., Tang, J.X., Yang, Z.S., and Duan, L.F. (2015) A genetic linkage between subduction- and collision-related porphyry Cu deposits in continental collision zones. Geology, 43, 247-250.

Hu, Y.B. (2015) Petrogenesis and metallogenetic implications of adakites in the Gangdese porphyry copper belt. A dissertation submitted to University of Chinese Academy of Sciences for the degree of doctor (in Chinese with English abstract).

Ishihara, S. (1981) The granitoid series and mineralization. Economic Geology, 75th Anniversary volume, 458-484.

Ishihara, S. (2015) Comparative studies of the petrochemistry of Sn-W-mineralized granitoids: Continent vs. island arc. Resource Geology, 3, 285-295.

Ji, W.Q., Wu, F.Y., Chung, S.L., Li, J.X., and Liu, Z.C. (2009) Zircon U-Pb geochronology and Hf isotopic constraints on petrogenesis of the Gangdese

batholith, southern Tibet. Chemical Geology, 262, 229-245.

Ji, W.Q., Wu, F.Y., Liu, X.C., Liu, Z.C., Zhang, C., Liu, T., Wang, J.G., and Paterson, S.R. (2020) Pervasive Miocene melting of thickened crust from the Lhasa terrane to Himalaya, Southern Tibet and its constraint on generation of Himalayan leucogranite. Geochimica et Cosmochimica Acta, 278, 137-156.

Jugo, P.J. (2009) Sulfur content at sulfide saturation in oxidized magmas. Geology, 37, 415-418.

Kang, D.Y., Zhang, Z.M., Palin, R.M., Tian, Z.L., and Dong, X. (2020) Prolonged partial melting of garnet amphibolite from the eastern Himalayan syntaxis: Implications for the tectonic evolution of large hot orogens. Journal of Geophysical Research: Solid Earth, 125: e2019JB019119.

Keppler, H. (1993) Influence of fluorine on the enrichment of high field strength trace elements in granitic rocks. Contributions to Mineralogy and Petrology, 114-479-488.

Lalonde, A.E., and Bernard, P. (1993) Composition and color of biotite from granites: two useful properties in characterization of plutonic suites from the Hepburn internal zone of Wopmay Orogen, Northwest Territories. The Canadian Mineralogist, 31: 203-217.

Lee, R.G., Byrne, K., D'Angelo, M., Hart, C.J.R., Hollings, P., Gleeson, S.A., and Alfaro, M. (2021) Using zircon trace element composition to assess porphyry copper potential of the Guichon Creek batholith and Highland Valley Copper deposit, south-central British Columbia. Mineralium Deposita, 56, 215-238.

Li, H.J., and Hermann, J. (2017) Chlorine and fluorine partitioning between apatite and

608 sediment melt at 2.5 GPa, 800 °C: a new experimentally derived thermodynamic
609 model. American Mineralogist, 102, 580-594.
610 Li, Q.Y., Yang, Z.M., Wang, R., Sun M.Y., and Qu, H.C. (2021) Zircon trace elemental
611 and Hf-O isotopic compositions of the Miocene magmatic suite in the giant Qulong
612 porphyry copper deposit, southern Tibet. Acta Petrologica et Mineralogica, 40,
613 1023-1048 (in Chinese with English abstract).
614 Liu, D., Zhao, Z.D., Zhu, D.C., Niu, Y.L., Depaolo, D.J., Harrison, T.M., Mo, X.X., Dong,
615 G.C., Zhou, S., Sun, C.G., Zhang, Z.C., and Liu, J.L. (2014) Postcollisional potassic
616 and ultrapotassic rocks in southern Tibet: Mantle and crustal origins in response to
617 India-Asia collision and convergence. Geochimica et Cosmochimica Acta, 143, 207-231.
618 Liu, Z.C., Wu, F.Y., Ji, W.Q., Wang, J.G., and Liu, C.Z. (2014) Petrogenesis of the Ramba
619 leucogranite in the Tethyan Himalaya and constraints on the channel flow mode.
620 Lithos, 208-209, 118-136.
621 Loader, M.A., Nathwani, C.L., Wilkinson, J.J., and Armstrong, R.N. (2022) Controls on
622 the magnitude of Ce anomalies in zircon. Geochimica et Cosmochimica Acta, 328,
623 242-257.
624 Loucks, R.R. (2014) Distinctive composition of copper-ore-forming arc magmas.
625 Australian Journal of Earth Sciences, 61, 5-16.
626 Loucks, R.R. Fiorentini, M.L., and Henríquez, G.J. (2020) New magmatic oxybarometer
627 using trace elements in zircon. Journal of Petrology, 61, 1-30.
628 Loucks, R.R. (2021) Deep entrapment of buoyant magmas by orogenic tectonic stress: Its

role in producing continental crust, adakites, and porphyry copper deposits. Earth-Science Reviews, 220, 103744.

Lu, Y.J., Loucks, R.R., Fiorentini, M.L., Yang, Z.M., and Hou, Z.Q. (2015) Fluid flux melting generated postcollisional high-Sr/Y copper ore-forming water-rich magmas in Tibet. Geology, 43, 1-14.

Lu, Y.J., Loucks, R.R., Fiorentini, M., McCuaig, T.C., Evans, N.J., Yang, Z.M., Hou, Z.Q., Kirkland, C.L., Parra-Avila, L.A., and Kobusee, A. (2016) Zircon composition as a pathfinder for porphyry Cu ± Mo ± Au deposits. Society of Economic Geologists, Special Publication, 19, 329-347.

Ma, L., Wang, Q., Wyman, D.A., Jiang, Z.Q., Yang, J.H., Li, Q.L., Gou, G.N., and Guo, H.F. (2013) Late Cretaceous crustal growth in the Gangdese area, southern Tibet: petrological and Sr-Nd-Hf-O isotopic evidence from Zhengga diorite-gabbro. Chemical Geology, 349, 54-70.

Mahoney, J.J., Frei, R., Tejada, M.L.G., Mo, X.X., Leat, P.T., and Nägler, T.F. (1998) Tracing the India ocean mantle domain though time: Isotopic results from old West Indian, East Tethyan and South Pacific seafloor. Journal of Petrology, 39, 1285-1306.

Marks, M.A.W., Scharrer, M., Ladenburger, S., and Markl, G. (2016) Comment on "Apatite: A new redox proxy for silicic magmas?". Geochimica et Cosmochimica Acta, 183, 267-270.

Mercer, C.N., and Reed, M.H. (2013) Porphyry Cu-Mo stockwork formation by dynamic,

transient hydrothermal pulses: Mineralogic insights from the deposit at Butte, Montana. Economic Geology, 108, 1347-1377.

Mo, X.X., Niu, Y.L., Dong, G.C., Zhao, Z.D., Hou, Z.Q., Zhou, S., and Ke, S. (2008) Contribution of syncollisional felsic magmatism to continental crust growth: A case study of the Paleogene Linzizong volcanic succession in southern Tibet: Chemical Geology, 250, 49-67.

Moshefi, P., Hosseinzadeh, M.R., Moayyed, M., and Lentz, D.R. (2018) Comparative study of mineral chemistry of four biotite types as geochemical indicators of mineralized and barren intrusions in the Sungun porphyry Cu-Mo deposit, northwestern Iran. Ore Geology Reviews, 97, 1-20.

Munoz, J.L. (1984) F-OH and Cl-OH exchange in micas with applications to hydrothermal ore deposits. Reviews in Mineralogy and Geochemistry, 13, 469-493.

O'Neill, H.S.C., Berry A.J., and Eggins, S.M. (2008) The solubility and oxidation stage of tungsten in silicate melts: implications for the comparative chemistry of W and Mo in planetary differentiation processes. Chemical Geology, 255, 346-359.

Rapp, R.P., and Watson, E.B. (1995) Dehydration melting of metabasalt at 8-32 kbar: Implications for continental growth and crust-mantle recycling. Journal of Petrology, 36: 891-931.

Richards, J.P. (2003) Tectono-magatic precursors for porphyry Cu-(Mo-Au) deposit formation. Economic Geology, 98, 1515-1533.

Richards, J.P. (2015) The oxidation state, and sulfur and Cu contents of arc magmas:

671 implications for metallogeny. Lithos, 233, 27-45.

672 Richards, J.P., and Kerrich, R. (2007) Adakite-like rocks: Their diverse origins and
673 questionable role in metallogenesis. Economic Geology, 102, 537-576.

674 Richards, J.P., Spell, T., Rameh, E., Razique, A., and Fletcher, T. (2012) High-Sr/Y
675 magmas reflect arc maturity, high magmatic water content, and porphyry Cu ± Mo ±
676 Au potential: Examples from the Tethyan arcs of central and eastern Iran and
677 western Pakistan. Economic Geology, 107, 295-332.

678 Rieder, M., Cavazzini, G., D'yakonov, Y.S., Frank-Kamenetskii, V.A., Gottardi, G.,
679 Guggeheim, S., Koval, P.W., Müeller, G., Neiva, A.M.R., Radoslovich, E.W., Robert
680 J.L., Sassi F.P., Takeda H., Weiss Z., and Wones D.R. (1998) Nomenclature of the
681 micas. Clays and Clay Minerals, 46, 586-595.

682 Sen, C., and Dunn, T. (1994) Dehydration melting of a basaltic composition amphibolites
683 at 1.5 and 2.0 GPa: Implications for the origin of adakites. Contributions to
684 Mineralogy and Petrology, 117: 394-409.

685 Sillitoe, R.H. (2010) Porphyry copper systems. Economic Geology, 105, 3-41.

686 Sisson, T.W., Ratajeski, K., Hankins, W.B., and Glazner, A.F. (2005) Voluminous granitic
687 magmas from common basaltic sources. Contributions to Mineralogy and Petrology,
688 148: 635-661.

689 Stock, M.J., Humpheys, M.C.S., Smith, V.C., Johnson, R.D., Pyle D.M., and Eimf. (2015)
690 New constraints on electron-beam induced halogen migration in apatite. American
691 Mineralogist, 100, 281-293.

692 Sun, X., Lu, Y.J., McCuaig, T.C., Zheng, Y.Y., Chang, H.F., Guo, F., and Xu, L.J. (2018)
693 Miocene ultrapotassic, high-Mg dioritic, and adakite-like rocks from Zhunuo in
694 southern Tibet: Implications for mantle metasomatism and porphyry copper
695 mineralization in collisional orogens. Journal of Petrology, 59, 341-386.
696 Tang, P., Tang, J.X., Wang, Y., Lin, B., Leng, Q.F., Zhang, Q.Z., He, L., Zhang, Z.B., Sun,
697 M., Wu, C.N., Qi, J., Li, Y.X., and Dai, S.J. (2021) Genesis of the Lakang'e
698 porphyry Mo (Cu) deposit, Tibet: Constraints from geochemistry, geochronology,
699 Sr-Nd-Pb-Hf isotopes, zircon and apatite. Lithos, 380-381, 105834.
700 Tang, P., Tang, J.X., Zheng, W.B., Leng, Q.F., Lin, B., and Tang, X.Q. (2017) Mineral
701 chemistry of hydrothermal biotites from the Lakange porphyry Cu-Mo deposit, Tibet.
702 Earth Science Frontiers, 24, 265-282 (in Chinese with English abstract).
703 Tian, F., Leng, C.B., Zhang, X.C., Tian, Z.D., and Zhang, W. (2021) The key role of
704 volatile-rich magma replenishment in the formation of porphyry Cu-Mo deposit: A
705 case study of Gangjiang porphyry Cu-Mo deposit, Tibet. Acta Petrologica Sinica, 37,
706 2889-2909 (in Chinese with English abstract).
707 Vigneresse, J.L. (2009) Evaluation of the chemical reactivity of the fluid phase through
708 hard-soft acid-base concepts in magmatic intrusions with applications to ore
709 generation. Chemical Geology, 263, 69-81.
710 Vigneresse, J.L., Duley, S., and Chattaraj, P.K. (2011) Describing the chemical character
711 of a magma. Chemical Geology, 287, 102-114.
712 Wang, L.Q., Wang, Y., Fan Y., and Danzhen W.X. (2018) A Miocene tungsten

713 mineralization and its implications in the western Bangong-Nujiang metallogenic
714 belt: Constraints from U-Pb, Ar-Ar, and Re-Os geochronology of the Jiaoxi tungsten,
715 Tibet, China. Ore Geology Reviews, 97, 74-87.
716 Wang, L.Q., Cheng, W.B., Gao, T., and Wang, Y. (2022) A model involving amphibolite
717 lower crust melting and subsequent melt extraction for leucogranite generation.
718 Geological Society of American Bulletin, 134, 1160-1179.
719 Wang, R., Richards, J.P., Hou, Z.Q., Yang, Z.M., Gou, Z.B., and Dufrane, S.A. (2014)
720 Increasing magmatic oxidation state from Paleocene to Miocene in the eastern
721 Gangdese belt, Tibet: Implication for collision-related porphyry Cu-Mo±Au
722 mineralization. Economic Geology, 109, 1943-1965.
723 Wang, R., Richards, J.P., Zhou, L., Hou, Z.Q., Stern R.A., Creaser, R.A., and Zhu, J.J.
724 (2015) The role of Indian and Tibetan lithosphere in spatial distribution of Cenozoic
725 magmatism and porphyry Cu-Mo deposits in the Gangdese belt, southern Tibet.
726 Earth-Science Reviews, 150, 68-94.
727 Wang, R., Weinerg, R.F., Collins, W.J., Richards, J.P., and Zhu, D.C. (2018) Origin of
728 postcollisional magmas and formation of porphyry Cu deposit in southern Tibet.
729 Earth-Science Reviews, 181, 122-143.
730 Wang, Y., Tang, J.X., Wang, L.Q., Huizenga, J.M., Santosh, M., Zheng, S.L., Hu, Y., and
731 Gao, T. (2020) Geology, geochronology and geochemistry of the Miocene Jiaoxi
732 quartz vein-type W deposit in the western part of the Lhasa Terrane, Tibet:
733 Implications for ore genesis. Ore Geology Reviews, 120, 103433.

734 Watson, E.B., and Harrison, T.M. (1983) Zircon saturation revisited: temperature and
735 composition effects in a variety of crustal magma types. Earth and Planetary Science
736 Letters, 64, 295-304.
737 Webster, J.D., and Piccoli, P.M. (2015) Magmatic apatite: A powerful, yet deceptive,
738 mineral. Elements, 11, 177-182.
739 Whitney, D.L., and Evans, B.W. (2010) Abbreviations for names of rock-forming
740 minerals. American Mineralogist, 95, 185-187.
741 Wu, S. (2016) The super-large Zhunuo porphyry Cu deposit in the Gangdese belt,
742 southern Tibet: magmatism and mineralization. A dissertation submitted to China
743 University of Geosciences for doctoral degree (in Chinese with English abstract).
744 Wu, S., Zheng, Y.Y., and Sun, X. (2016). Subduction metasomatism and collision-related
745 metamorphic dehydration controls on the fertility of porphyry copper ore-forming
746 high-Sr/Y magma in Tibet. Ore Geology Review, 73, 83-103.
747 Xiang, H. and Connolly, J.A.D. (2022) GeoPS: An interactive visual computing tool for
748 thermodynamic modelling of phase. Journal of Metamorphic Geology, 40: 243-255.
749 Xiao, B., Qin, K.Z., Li, G.M., Li, J.X., Xia, D.X., Chen, L., and Zhao, J.X. (2011) Highly
750 oxidized magma and fluid evolution of Miocene Qulong giant porphyry Cu-Mo
751 deposit, southern Tibet, China. Resource Geology, 62, 4-18.
752 Yang, Z.M., Lu, Y.J., Hou, Z.Q., and Chang, Z.S. (2015) High-Mg diorite from Qulong in
753 southern Tibet: Implications for the genesis of Adakite-like intrusions and associated
754 porphyry Cu deposits in collisional orogens. Journal of Petrology, 56, 227-254.

755 Yang, Z.M., Goldfarb, R., and Chang, Z.S. (2016) Generation of postcollisional porphyry
756 copper deposits in southern Tibet triggered by subduction of the Indian continental
757 plate. Economic Geology, S19, 279-300.
758 Yu, K.L., Li, G.M., Zhao, J.X., Evans, N.J., Li, J.X., Jiang, G.W., Zou, X.Y., Qin, K.Z.,
759 and Guo, H. (2022) Biotite compositions as a tracer of fluid evolution and
760 mineralization center: a case study at the Qulong porphyry Cu-Mo deposit, Tibet.
761 Mineralium Deposita, 57: 1047-1069.
762 Zeng, L.S., Gao, L.E., Xie, K.J., and Liu, Z.J. (2011) Mid-Eocene high-Sr/Y granites in
763 the Northern Himalayan Gneiss Domes: Melting thickened lower continental crust.
764 Earth and Planetary Science Letters, 303, 251-266.
765 Zeng, L.S., Gao, L.E., Tang, S.H., Hou, K.J., Guo, C.L., and Hu, G.Y. (2014) Eocene
766 magmatism in the Tethyan Himalaya, southern Tibet, in Mukherjee, S., Carosi, R.,
767 van der Beek, P.A., Mukherjee, B.K., and Robinson, D.M., eds, Tectonics of the
768 Himalayan. Geological Society, London, Special Publication, 412, 287-316.
769 Zhang, S.Q., Mahoney, J.J., Mo, X.X., Ghazi, A.M., Milani, L., Crawford, A.J., Guo, T.Y.,
770 and Zhao, Z.D. (2005). Evidence for a widespread Tethyan upper mantle with
771 Indian-Ocean-type isotopic characteristics. Journal of Petrology, 46, 829-858.
772 Zhang, Z.B. (2021) The Jiama copper-polymetallic deposit in Tibet: Magmatism,
773 diagenetic-metallogenic model. A dissertation submitted to China University of
774 Geosciences for Doctoral Degree (in Chinese with English abstract).
775 Zhang, Z.B., Wang, L.Q., Tang, P., Lin, B., Sun, M., Qi, J., Li, Y.X., and Yang, Z.K.

(2020) Geochemistry and zircon trace elements composition of the Miocene ore-bearing biotite monzogranite porphyry in the Demingding porphyry Cu-Mo deposit, Tibet: Petrogenesis and implication for magma fertility. Geological Journal, 55, 4525-4542.

Zheng, Y.C., Wu, C.D., Tian, S.H., Hou, Z.Q., and Fu, B. (2020) Magmatic and structural controls on the tonnage and metal association of collision-related porphyry copper deposits in southern Tibet. Ore Geology Reviews, 122, 103509.

Zhu, D.C., Zhao, Z.D., Niu, Y.L., Dilek, Y., Hou, Z.Q., and Mo, X.X. (2013) The origin and pre-Cenozoic evolution of the Tibetan plateau. Gondwana Research, 23, 1429-1454.

Zhu, D.C., Li, S.M., Cawood, P.A., Wang, Q., Zhao, Z.D., Liu, S.A., and Wang, L.Q. (2016) Assembly of the Lhasa and Qiangtang terranes in central Tibet by divergent double subduction. Lithos, 245, 7-17.

Zhu, J.J., Richards, J.P., Rees, C., Creaser, R., DuFrane, A.A., Locock, A., Petrus, J.A., and Lang, J. (2018) Elevated magmatic sulfur and chlorine contents in ore-forming magmas at the Red Chris porphyry Cu-Au deposit, northern British Columbia, Canada. Economic Geology, 113, 1047-1075.

Zou, X.Y., Qin, K.Z., Han, X.L., Li, G.M., Evans, N.J., Li, Z.Z., and Yang, W. (2019) Insight into zircon REE oxy-barometers: A lattice strain model perspective. Earth and Planetary Science Letters, 506, 87-96.

FIGURE CAPTIONS

FIGURE 1. Simplified geological map of the Lhasa terrane showing tectonic units (a) and spatial distributions of the Miocene PCDs and the W mineralized areas (b; modified after Zhu et al. 2013). BNSZ = Bangong-Nujiang suture zone; SNMZ = Shiquan River-Nam Tso mélange zone; LMF = Luobadui-Milashan fault; KF = Karakorum fault; IYZS = Indus-Yarlung Zangbo suture zone; MBT = Main boundary thrust; MCT = Main central thrust; STDS = South Tibet detachment system.

FIGURE 2. Diagrams showing the high-Sr/Y **(a)** and high-La/Yb **(b)** features of the Miocene Gangdese Cu and W granitoids. The data for the Cu granitoids are from Zheng et al. (2020) and references therein; the data for the W granites are from Wang Y. et al. (2020) and Wang L.Q. et al. (2022).

FIGURE 3. Petrographic characteristics of the Miocene Gangdese W granites. (**a**) Cross polarized light (CPL) photomicrograph of the Jiaoxi biotite monzogranite. (**b**) Backscattered electron (BSE) image of biotite with apatite and ilmenite inclusions from the Jiaoxi biotite monzogranite. (**c and d)** Subhedral apatite crystals in biotite from biotite monzogranite. (**e**) Cathodoluminescence (CL) images of zircons in the Jiaoxi biotite monzogranite (Wang L.Q. et al. 2018). (**f**) Plane-polarized light (PPL) photomicrograph of Jiaodong two-mica granite. (**g**) BSE images of biotite and apatite from the Jiaodong two-mica granite. (**h and i**) Euhedral crystals and homogeneous textures of apatite in the groundmass (h) and biotite (i) of the Jiaodong two-mica granite. (**j**) CL images of zircons from the Jiaodong biotite monzogranite (Wang L.Q. et al. 2018).

(**k**) Photomicrograph of the Anglonggangri two-mica granite. (**l**) BSE images of biotite and apatite from the Anglonggangri two-mica granite. (**m and n**) Euhedral and homogeneous apatite crystals hosted in the matrix (m) and biotite (n) in Anglonggangri two-mica granite. (**o**) CL images of zircons from the Anglonggangri two-mica granite (Wang L.Q. et al. 2022). Hereafter, mineral abbreviations follow Whitney and Evans (2010). Ap-apatite; Bt-biotite; Ms-muscovite; Mnz-monazite; Pl-plagioclase; Qz-quartz; Kfs-K-feldspar; Ilm-ilmenite; Zrn-zircon.

FIGURE 4. Diagrams showing F, Cl and SO_3 abundances in biotite from the Gangdese W and Cu granitoids. **(a)** SO_3 vs. Cl, **(b)** Cl vs. F, and **(c)** F/Cl vs. F diagrams. **(d)** The classification diagram of biotite. The PCD data are from Wu et al. (2016), Tang et al. (2017), Sun et al. (2018), Tian et al. (2021), Zhang (2021) and Yu et al. (2022).

FIGURE 5. Diagrams showing the F, Cl and SO_3 contents of apatite from the Gangdese W and Cu granitoids. (**a**) Cl vs. F, (**b**) F/Cl vs. F, (**c**) SO_3 vs. F, and (**d**) SO_3 vs. Cl diagrams. Reference lines are given at the estimated break between the W and Cu granitoids. The PCD data are from Xiao et al. (2011), Hu (2015), Wu (2016), Wu et al. (2016), Tang et al. (2021), Tian et al. (2021) and Zhang (2021).

FIGURE 6. Diagrams for fO_2 of the Gangdese W and Cu granitoids. (**a**) Bulk-rock Fe_2O_3/FeO vs. SiO_2 diagram (modified from Hart et al. 2004). (**b**) LogfO_2 vs. temperature diagram for zircon. (**c**) Zircon ΔFMQ vs. $T_{Ti\text{-}Zr}$ diagram. QFM = quartz-fayalite-magnetite; NNO = nickel-nickel oxide; Hem-Mag = hematite-magnetite; IW = Fe wüsite; QIF = quartz-iron-fayalite. The Fe_2O_3 and FeO data for the PCDs are the same as those in Fig. 2.

839 Data on PCD zircons are from Wang R. et al. (2014), Hu (2015), Wu et al. (2016), Sun et
840 al. (2018), Zhang et al. (2020), Tang et al. (2021), Li et al. (2021) and Zhang (2021).

841 **Figure 7.** (**a-c**) Trace element compositions of zircon showing the relative H_2O content in
842 the W and Cu granitoids. (**a**) Eu/Eu^* vs. (Ce/Nd)/Y, (**b**) Ce/Nd vs. Dy/Yb, (**c**) Eu/Eu^* vs.
843 Dy/Yb. The reference lines are from Lu et al. (2016) and Lee et al. (2021) and indicate
844 different H_2O contents in the Cu and W granitoids. The data for the PCDs are the same as
845 those in Fig. 6. (**d**) Diagram showing magma H_2O content estimated for the W granites.

846 **FIGURE 8.** IV(F) vs. IV(F/Cl) diagram shows the halogen content of biotite from the W
847 granites. Fields of porphyry Cu and Mo and Sn-W-Be deposits are from Munoz (1984).

848 **FIGURE 9.** (a) Zircon $\varepsilon_{Hf}(t)$ vs. U-Pb ages; (b) zircon Hf isotope T_{DM}^{C} vs. U-Pb ages; (c)
849 $(^{87}Sr/^{86}Sr)_i$ vs. SiO_2; and (d) $\varepsilon_{Nd}(t)$ vs. $(^{87}Sr/^{86}Sr)_i$ diagrams for the Gangdese Cu and W
850 granitoids. The data for the PCD and W granitoids are the same as those in Fig. 2. Other
851 Sr-Nd isotope sources include the Yarlung Zangbo Ophiolite from Mahoney et al. (1998)
852 and Zhang et al. (2005); gabbro 09TB79 from Ma et al. (2013); gneiss G118A and
853 G118D from Harris et al. (1988a, b); Himalayan Eocene two-mica granite from Zeng et al.
854 (2011, 2014) and Hou et al. (2012); and Himalayan Miocene leucogranite and
855 metasediment from Ji et al. (2020) and Liu Z.C. et al. (2014) and references within.

856 **FIGURE10.** Cartoon illustrating the petrogenetic differences between the Miocene
857 Gangdese Cu and W granitoids.

This is the peer-reviewed, final accepted version for American Mineralogist, published by the Mineralogical Society of America.
The published version is subject to change. Cite as Authors (Year) Title. American Mineralogist, in press.
DOI: https://doi.org/10.2138/am-2023-9023. http://www.minsocam.org/

TABLE 1. Comparison of key parameters between the Gangdese W granites and Cu granitoids

Granitoids		Temperature/°C	fO_2			H_2O content			Halogen contents/wt.%		
		T_{Ti-Zr}	log fO_2	ΔFMQ	Bulk-rock Fe_2O_3/FeO	wt.%	(Ce/Nd)/Y	Dy/Yb	F	Cl	SO_3
W granites	Biotite monzogranite	653-876 Aver = 777	-19.6~-13.8 Aver = -15.5	-2.1~2.4 Aver = 0.2	0.14-0.32 Aver = 0.22	7-9	0.001-0.028 half < 0.01	> 0.3	Ap: 2.48-3.75 Aver = 3.05	Ap: 0.009	Ap: 0.031
	Two-mica granite	721-840 Aver = 777	-21.4~-14.1 Aver = -16.3	-2.2~0.6 Aver = -0.8	0.13-0.32 Aver = 0.20				Bt: 0.40-1.71 Aver = 1.02 Ap: 1.44-3.65 Aver = 2.69	Bt: 0.009-0.193 Aver = 0.021 Ap: 0.009-0.041 Aver = 0.017	Bt: 0.020-0.069 Aver = 0.029 Ap: 0.020-0.379 most < DL
Cu granitoids		651-873 Aver = 686	-18.6~-12.2 Aver = -16.1	-0.8~4.1 Aver = 1.6	0.08-7.87 Aver = 1.34	10-12	> 0.01	most < 0.3	Bt: 0.04-1.91 Aver = 0.62 Ap: 1.37-3.73 Aver = 2.68	Bt: most > 0.03 Ap: most > 0.05	Ap: most > 0.04

Note: Aver-average; Ap-apatite; Bt-biotite; D-detection limit.

This is the peer-reviewed, final accepted version for American Mineralogist, published by the Mineralogical Society of America.
The published version is subject to change. Cite as Authors (Year) Title. American Mineralogist, in press.
DOI: https://doi.org/10.2138/am-2023-9023. http://www.minsocam.org/

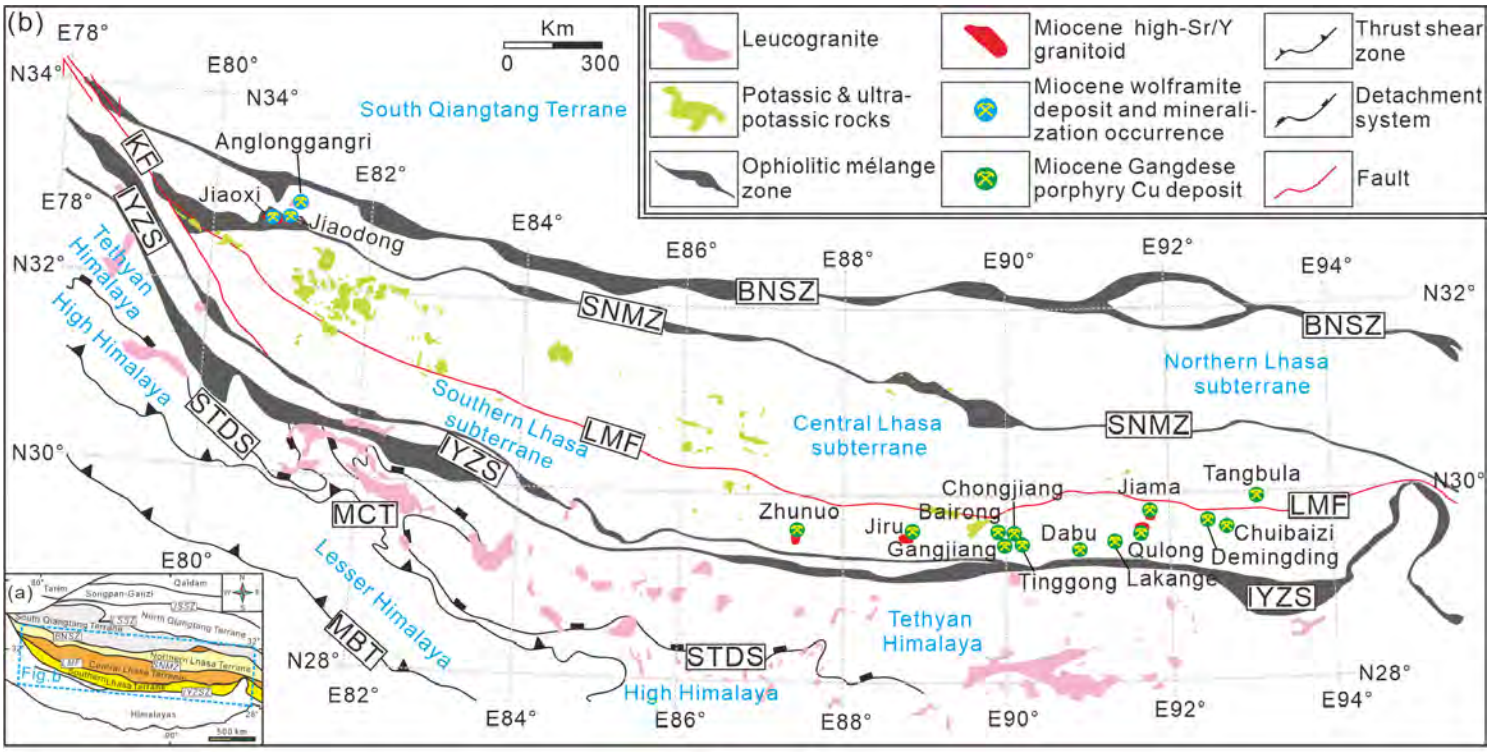

Figure 1

This is the peer-reviewed, final accepted version for American Mineralogist, published by the Mineralogical Society of America.
The published version is subject to change. Cite as Authors (Year) Title. American Mineralogist, in press.
DOI: https://doi.org/10.2138/am-2023-9023. http://www.minsocam.org/

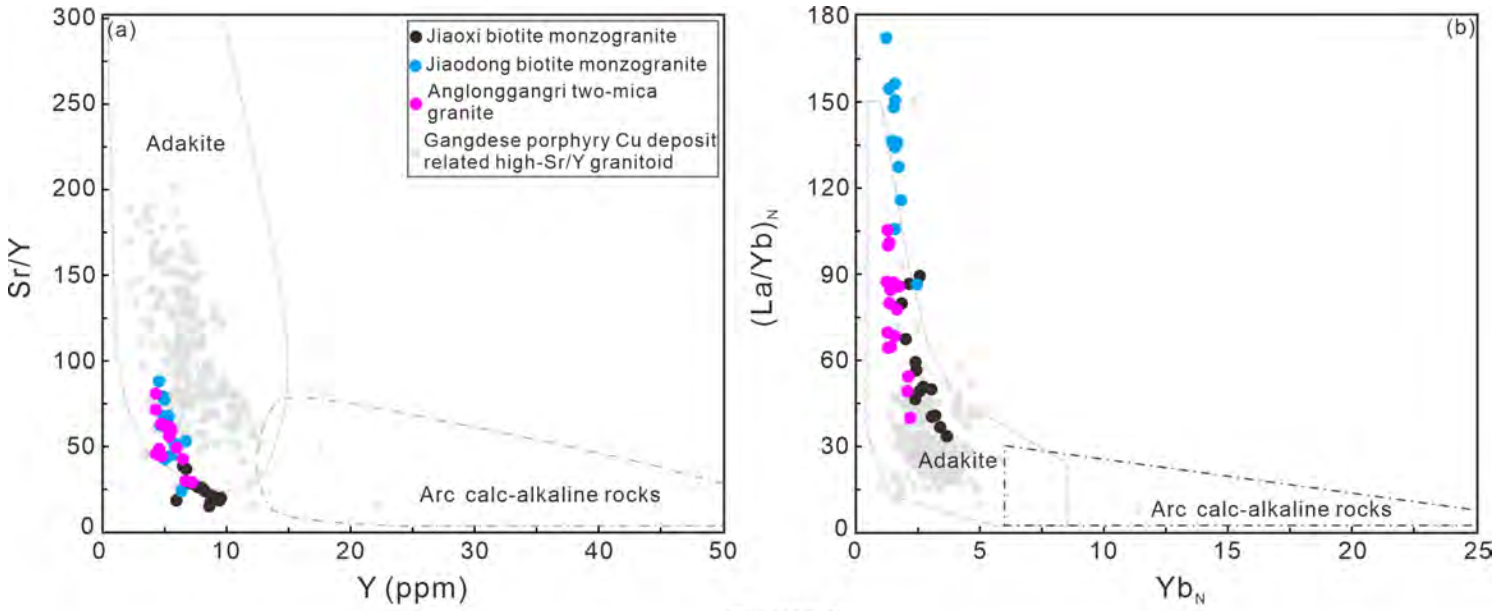

Figure 2

This is the peer-reviewed, final accepted version for American Mineralogist, published by the Mineralogical Society of America.
The published version is subject to change. Cite as Authors (Year) Title. American Mineralogist, in press.
DOI: https://doi.org/10.2138/am-2023-9023. http://www.minsocam.org/

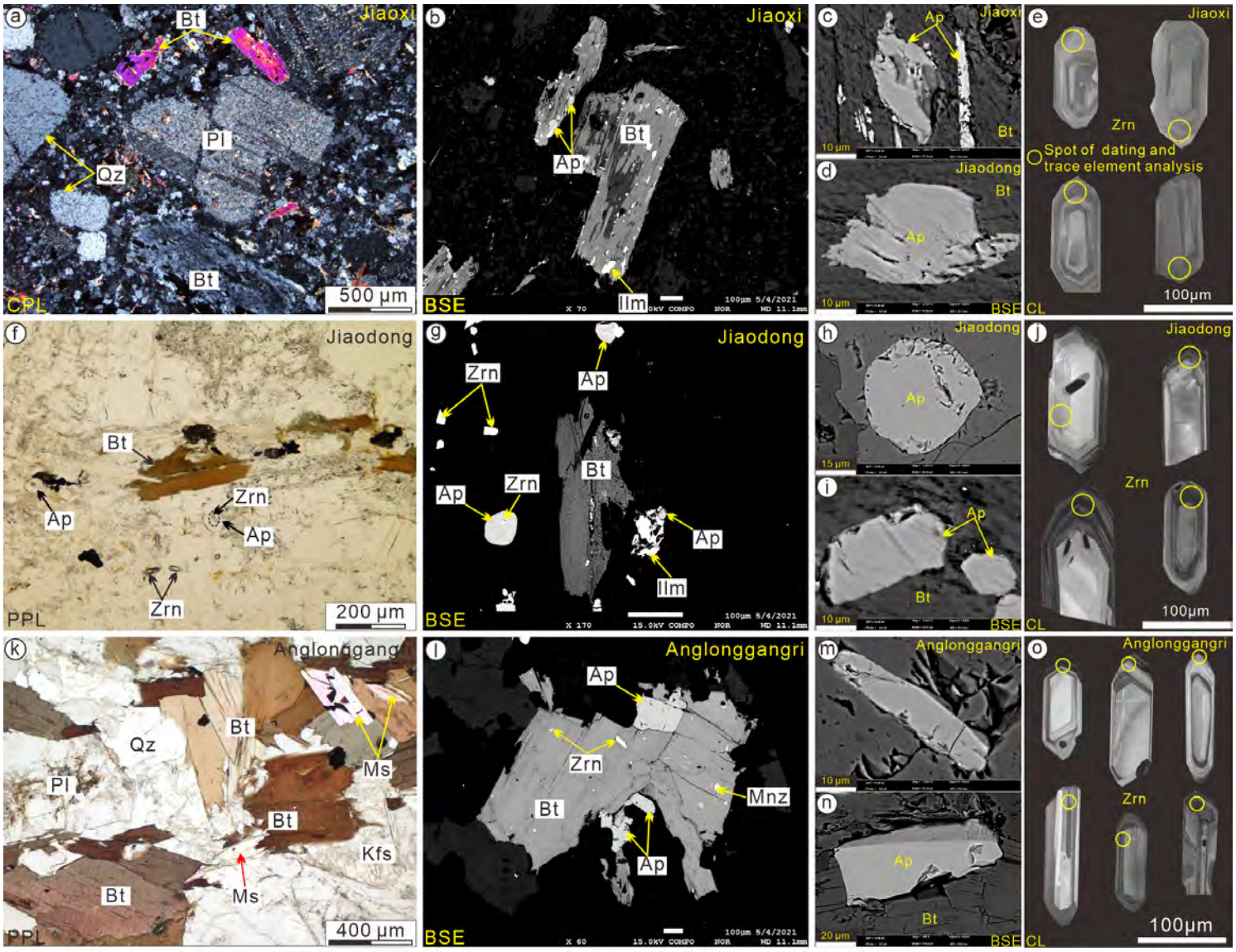

Figure 3

This is the peer-reviewed, final accepted version for American Mineralogist, published by the Mineralogical Society of America.
The published version is subject to change. Cite as Authors (Year) Title. American Mineralogist, in press.
DOI: https://doi.org/10.2138/am-2023-9023. http://www.minsocam.org/

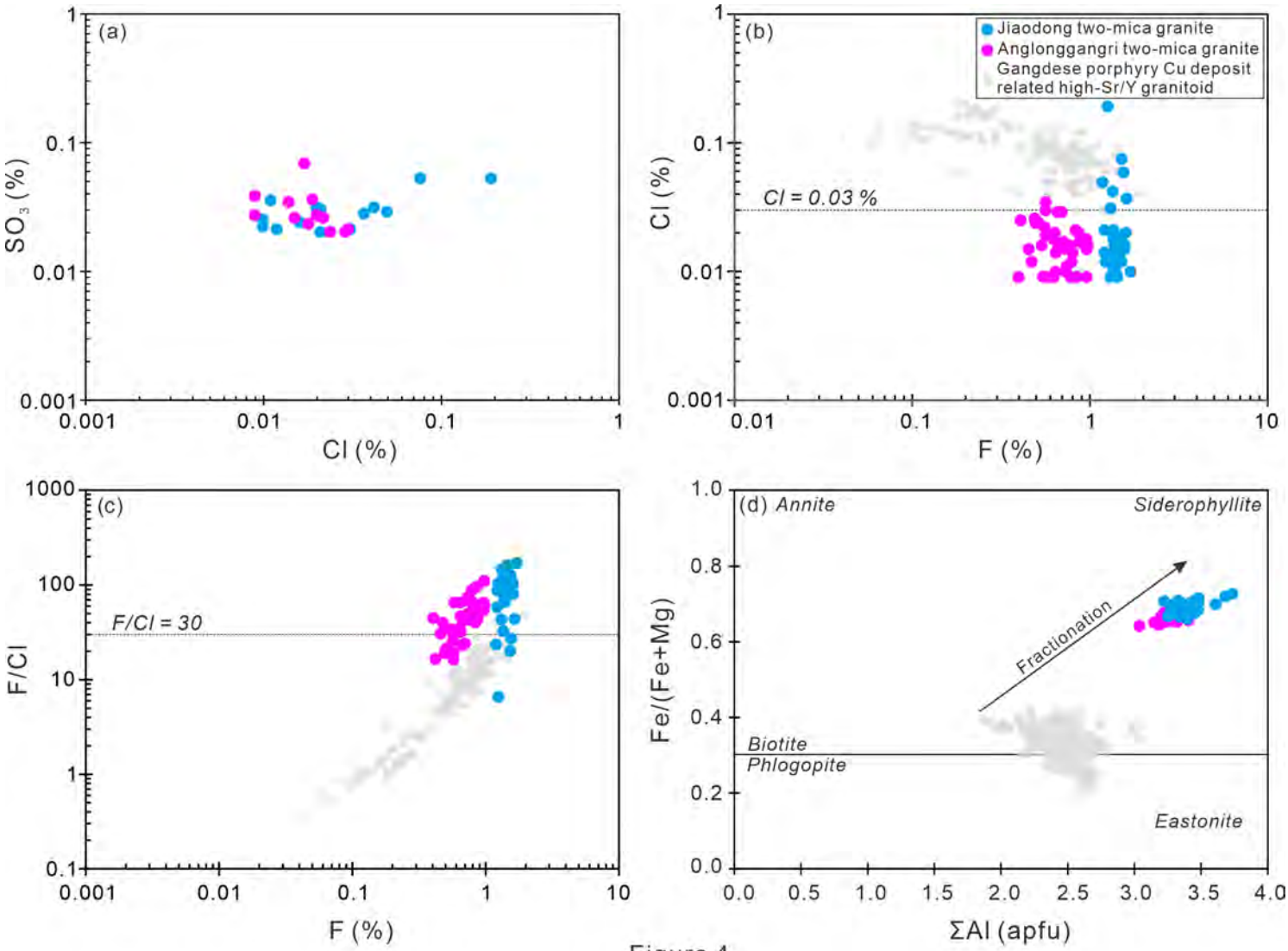

Figure 4

This is the peer-reviewed, final accepted version for American Mineralogist, published by the Mineralogical Society of America.
The published version is subject to change. Cite as Authors (Year) Title. American Mineralogist, in press.
DOI: https://doi.org/10.2138/am-2023-9023. http://www.minsocam.org/

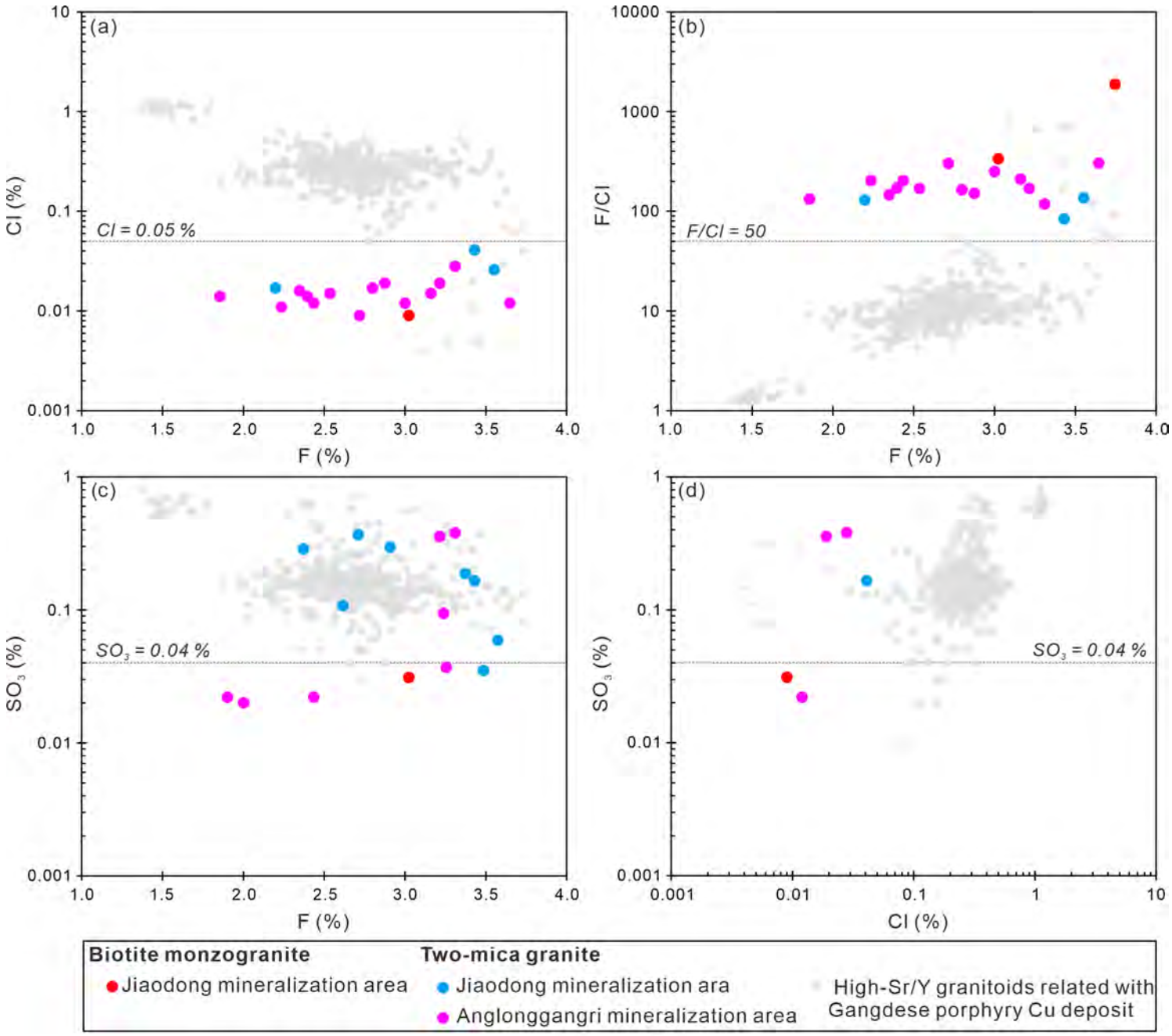

Figure 5

This is the peer-reviewed, final accepted version for American Mineralogist, published by the Mineralogical Society of America.
The published version is subject to change. Cite as Authors (Year) Title. American Mineralogist, in press.
DOI: https://doi.org/10.2138/am-2023-9023. http://www.minsocam.org/

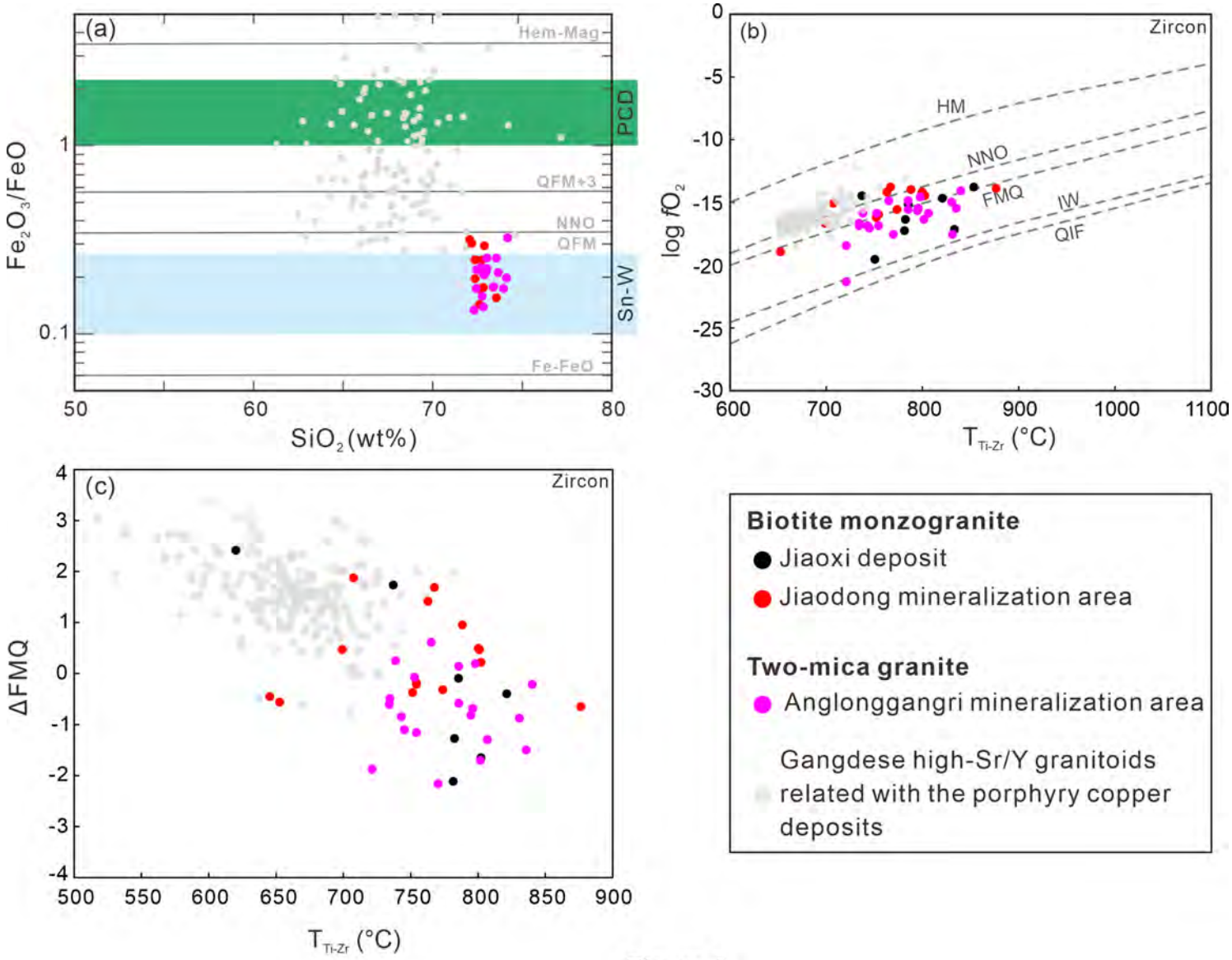

Figure 6

This is the peer-reviewed, final accepted version for American Mineralogist, published by the Mineralogical Society of America.
The published version is subject to change. Cite as Authors (Year) Title. American Mineralogist, in press.
DOI: https://doi.org/10.2138/am-2023-9023. http://www.minsocam.org/

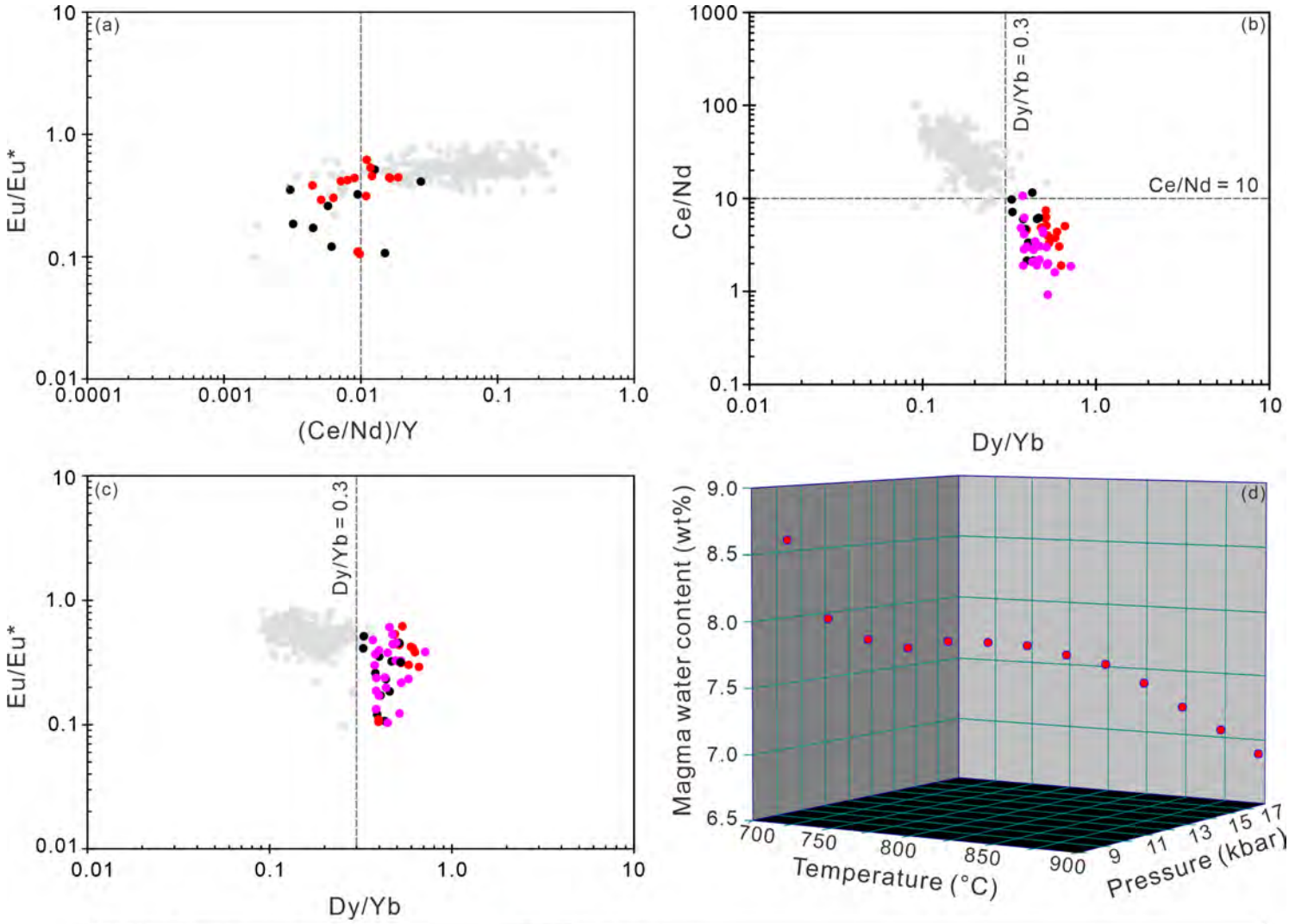

Figure 7

This is the peer-reviewed, final accepted version for American Mineralogist, published by the Mineralogical Society of America.
The published version is subject to change. Cite as Authors (Year) Title. American Mineralogist, in press.
DOI: https://doi.org/10.2138/am-2023-9023. http://www.minsocam.org/

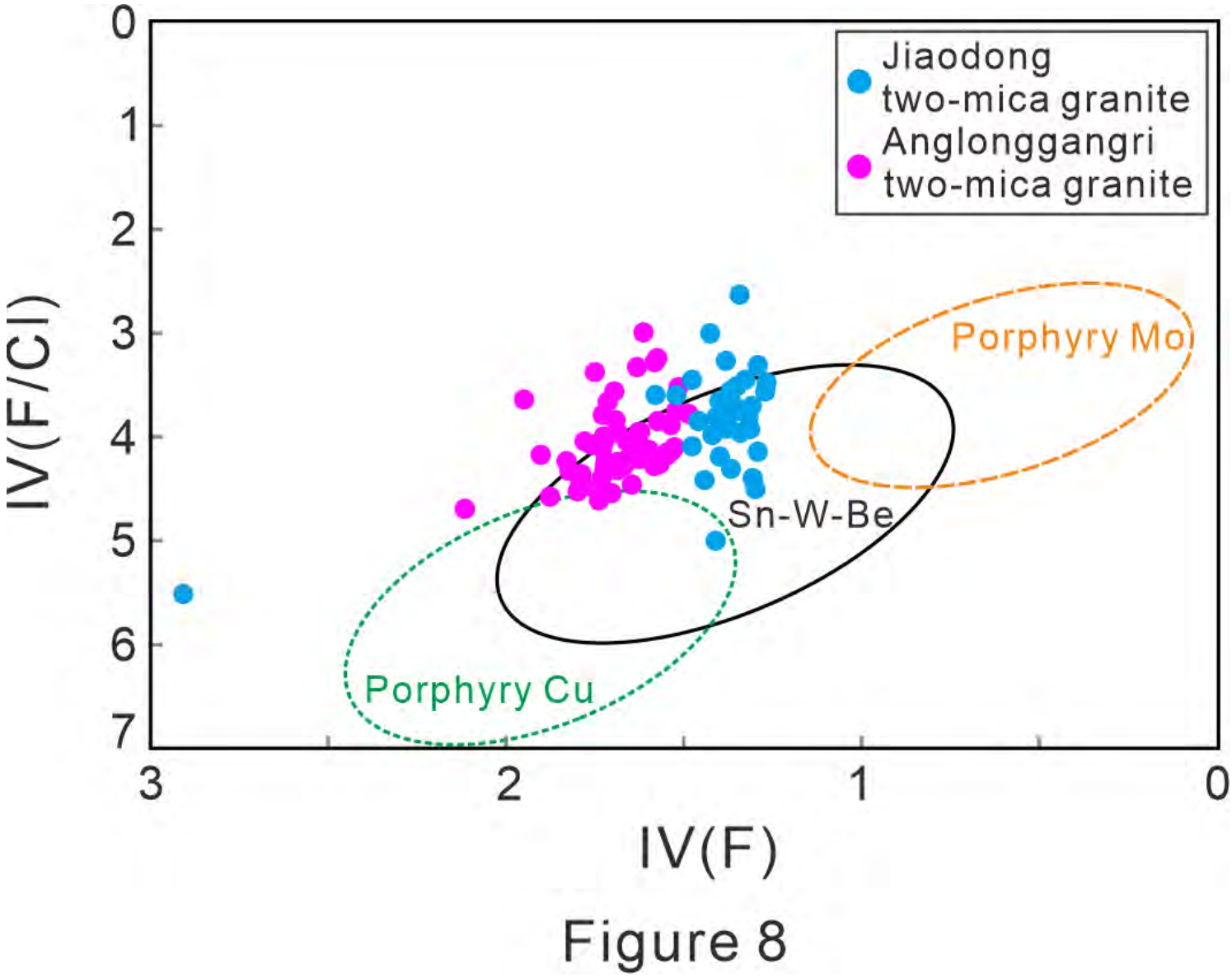

Figure 8

This is the peer-reviewed, final accepted version for American Mineralogist, published by the Mineralogical Society of America.
The published version is subject to change. Cite as Authors (Year) Title. American Mineralogist, in press.
DOI: https://doi.org/10.2138/am-2023-9023. http://www.minsocam.org/

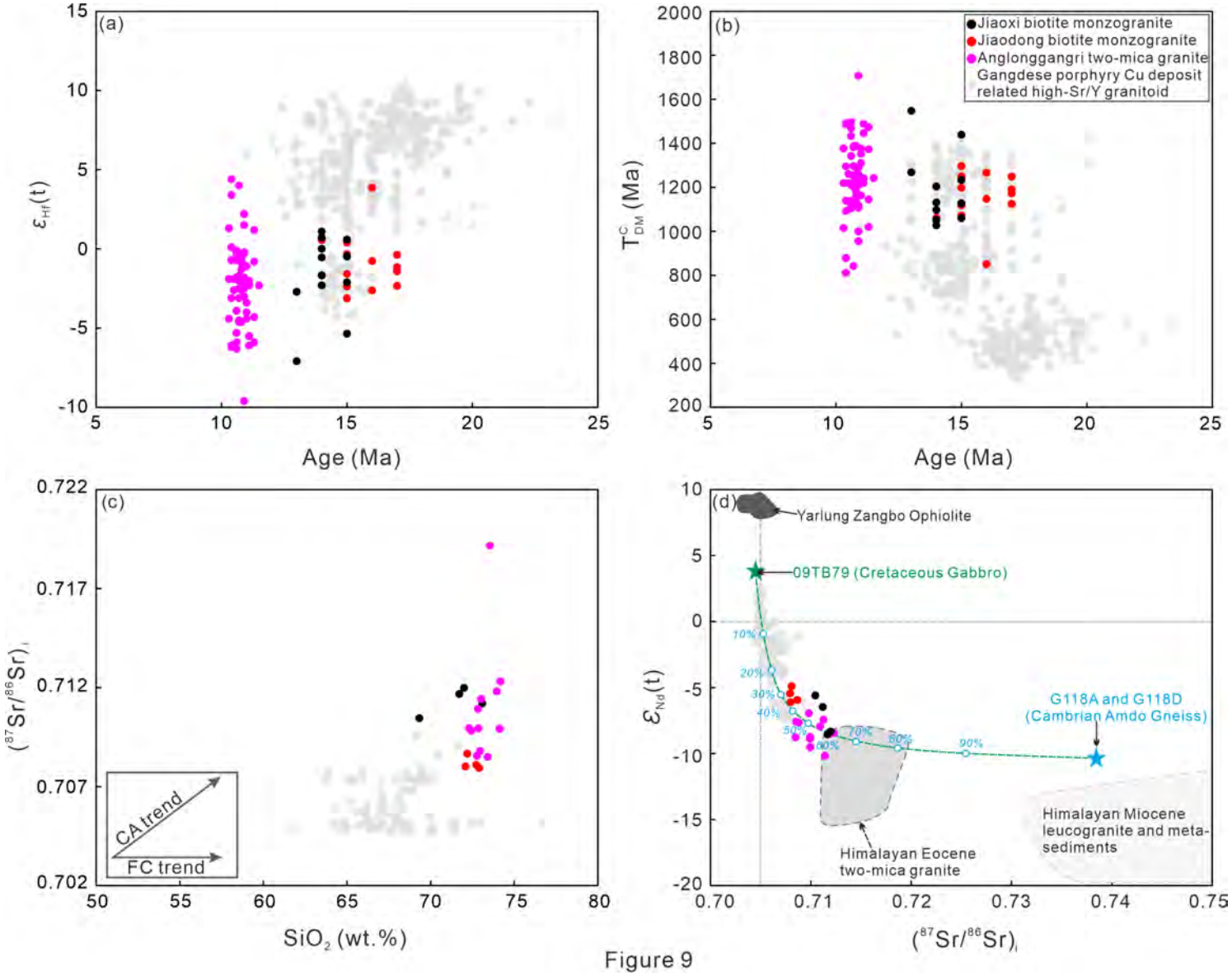

Figure 9

This is the peer-reviewed, final accepted version for American Mineralogist, published by the Mineralogical Society of America.
The published version is subject to change. Cite as Authors (Year) Title. American Mineralogist, in press.
DOI: https://doi.org/10.2138/am-2023-9023. http://www.minsocam.org/

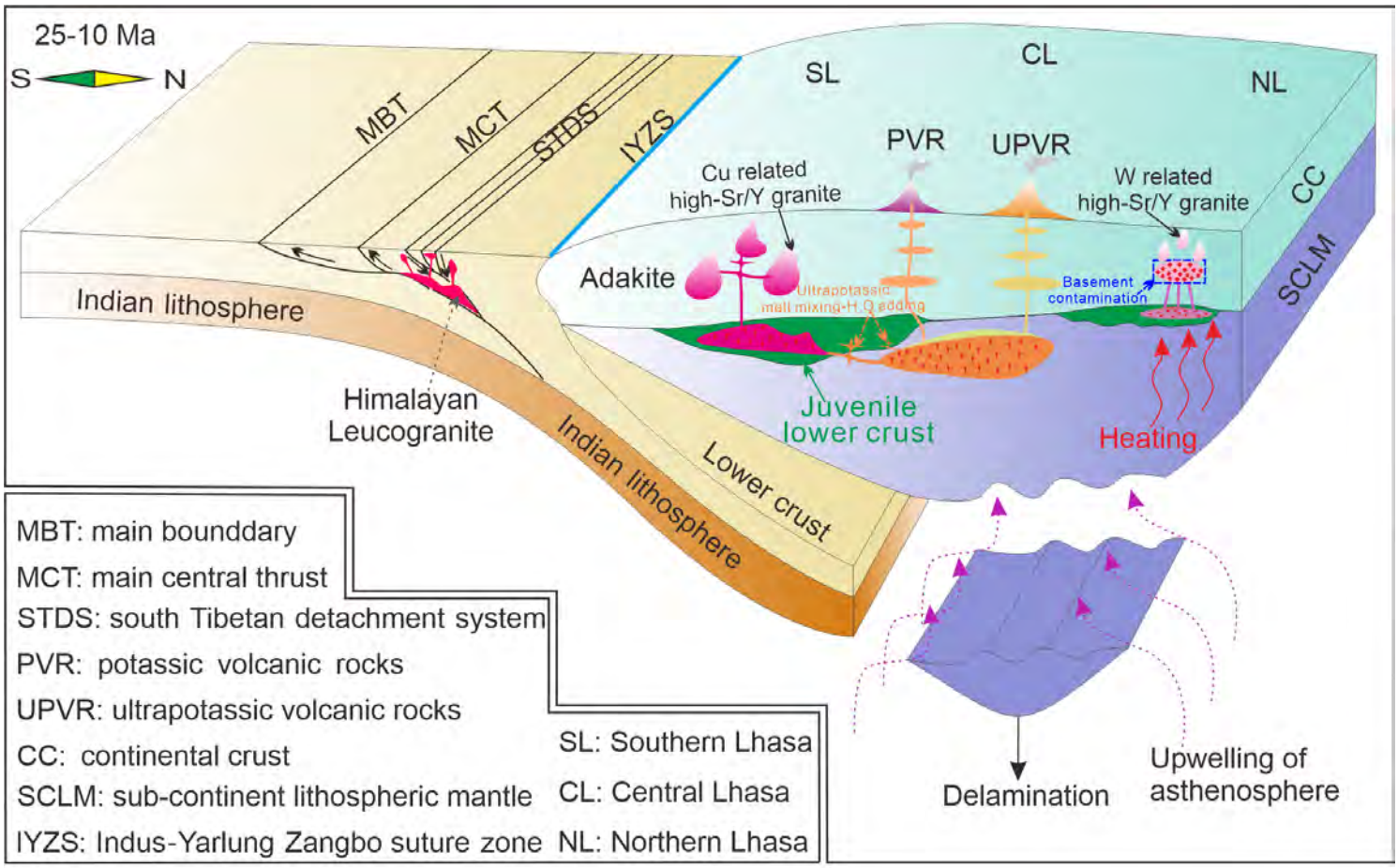

Figure 10